

# Chapter 6

## Macroscopic Manifestations of Hydrogen Embrittlement



Hydrogen embrittlement appears as cracking or premature fracture during service or mechanical testing, and environmental and testing conditions are crucial to the evolution. Blistering is induced under high hydrogen fugacity even without external stress, but degradation or eventual failure of structural steel components usually emerges under applied stress in mild environments. The function of hydrogen in the degradation is coupled with applied stress and plastic strain. This chapter presents primarily phenomenological manifestations of hydrogen effects in various mechanical tests of steels.

### 6.1 Tensile Tests

#### 6.1.1 Effects of Test Conditions

In tensile tests using bulky specimens, hydrogen degradation appears as premature fracture after or eventually before necking, the seemingly elastic region close to the yield stress, according to materials, hydrogen concentrations, and stress conditions. The degradation is expressed in terms of the fracture stress, the elongation to fracture, and the reduction in area.

##### 6.1.1.1 Hydrogen Concentration

Two methods, concurrent with or prior to testing, are used to introduce hydrogen into specimens, and the resultant degradation is not the same according to the method. Figure 6.1 [1] shows stress–strain curves of the same steel hydrogen precharged to different concentrations. Varied hydrogen concentrations did not affect the flow stress, but an earlier fracture occurred in higher hydrogen concentrations. The steel (0.84C–0.19Si–0.76Mn in %) was a lower bainitic bar 3 mm in diameter, 1517 MPa in

© The Author(s), under exclusive license to Springer Nature Singapore Pte Ltd. 2023 123  
M. Nagumo, *Fundamentals of Hydrogen Embrittlement*,  
[https://doi.org/10.1007/978-981-99-0992-6\\_6](https://doi.org/10.1007/978-981-99-0992-6_6)

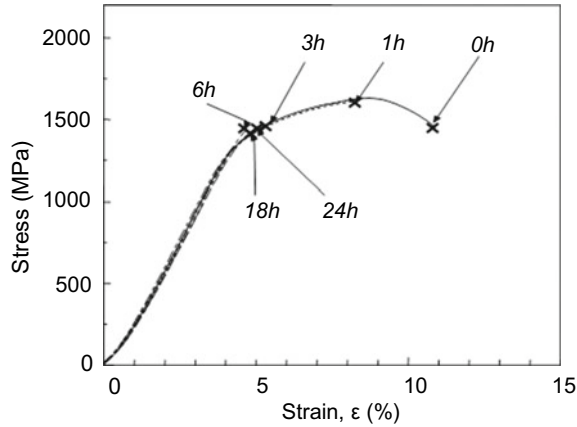


**Fig. 6.1** Tensile stress–strain curve of a high-strength lower-bainitic steel with/without hydrogen precharging by immersion in 20%  $\text{NH}_4\text{SCN}$  solution at 323 K for various periods. Test at room temperature at a strain rate of  $5 \times 10^{-7}/\text{s}$  (Takai et al. [1]. Reprinted with permission from The Iron and Steel Institute Japan)

tensile strength. Hydrogen precharging was immersing specimens in a 20% aqueous solution of  $\text{NH}_4\text{SCN}$  at 323 K for various periods. The tensile tests were at room temperature with a strain rate of  $5 \times 10^{-7}/\text{s}$ .

The hydrogen concentration increased with the immersion time to saturate at about 3 mass ppm after 10 h. Thermal desorption analysis (TDA) profiles of hydrogen exhibited a single desorption-rate peak at around 393 K, suggesting that hydrogen is weakly trapped in lattice defects as described in Sect. 2.1.2. In fact, hydrogen almost totally diffused out at room temperature in 800 h.

Trapped states of hydrogen in materials alter the dependence of degradation on the hydrogen concentration. Strong and weak hydrogen trapping sites were prepared in the steel of the same compositions as Fig. 6.1 by isothermal transformation at 823 K to eutectoid structure, followed by cold-drawing to 85% reduction in area [1]. TDA profiles of hydrogen, precharged in the same way as for Fig. 6.1, exhibited two peaks at around 393 K (Peak<sup>#1</sup>) and 823 K (Peak<sup>#2</sup>), similar to Fig. 2.8. Specimens that contain only Peak<sup>#2</sup> hydrogen were prepared by annealing the cold-drawn and hydrogen-charged specimens at 473 K. Hydrogen composing Peak<sup>#2</sup> is strongly trapped and non-diffusive even at 473 K. Figure 6.2(a) shows the relative reduction of area at tensile tests of specimens containing both Peak<sup>#1</sup> and Peak<sup>#2</sup> and only Peak<sup>#2</sup> [2]. The reference specimens were without hydrogen precharging, and Fig. 6.2(a) shows that hydrogen composing Peak<sup>#2</sup> is immune to the degradation, implying that *the total hydrogen content does not serve as a parameter for the degradation of tensile properties*.

Figure 6.2(b) shows the increase in tracer hydrogen  $C_{\text{H}}$ , i.e., hydrogen introduced as a tracer of lattice defects, described in Sect. 3.1.1.3 concerning Fig. 3.2. The hydrogen effect enhancing the strain-induced generation of defects is expressed by

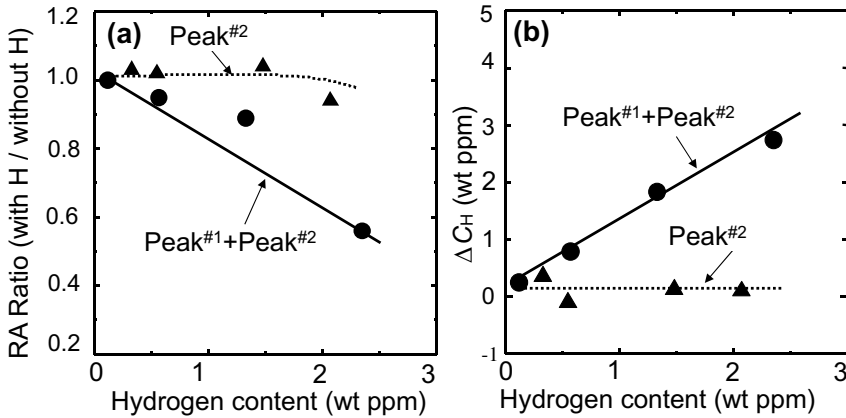


**Fig. 6.2** (a) Relative reduction of area (RA) and (b)  $\Delta C_H$  as a function of the strain rate at 323 K of specimens containing (Peak<sup>#1</sup> + Peak<sup>#2</sup>) and only Peak<sup>#2</sup>. Peak<sup>#1</sup> and Peak<sup>#2</sup> hydrogen are 1.9 and 2.6 mass ppm, respectively (Doshida et al. [2])

$\Delta C_H$ , defined as the difference in tracer-hydrogen between specimens strained to 0.08 with and without hydrogen.  $\Delta C_H$  was almost null in specimens showing only Peak<sup>#2</sup> hydrogen. It again implies that hydrogen composing Peak<sup>#2</sup> does not enhance the strain-induced generation of lattice defects.

### 6.1.1.2 Temperature and Strain Rate

Strain-rate and testing temperature dependencies characterize the susceptibility to hydrogen embrittlement of steel in tensile tests. Figure 6.3 [3] schematically illustrates the dependencies of fracture strain in terms of the reduction in area at fracture for mild steel. The degradation is the most prominent at around room temperature and with decreasing strain rates. A common understanding of the origin is the buildup rate of local hydrogen concentration through diffusion. However, studies on the origin using TDA gave information on the states of hydrogen in materials [2].

As shown in Fig. 2.8 and the preceding section, hydrogen introduced into cold-drawn eutectoid steel bars exhibited two thermal desorption-rate peaks, Peak<sup>#1</sup> and Peak<sup>#2</sup>. Tensile test results for the two series of specimens, one containing both Peak<sup>#1</sup> and Peak<sup>#2</sup> and the other containing only Peak<sup>#2</sup>, are shown in Fig. 6.4(a) for various strain rates [2]. The ordinate denotes the ratio of the reduction in area at tensile tests of steels with and without hydrogen precharging. Hydrogen degradation and a strong strain-rate dependence of tensile ductility appeared for specimens containing Peak<sup>#1</sup> hydrogen, while specimens containing only Peak<sup>#2</sup> were almost immune.

The amounts of lattice defects newly created during tensile straining were evaluated in terms of the amount of tracer-hydrogen introduced after tensile straining. Similar to Figs. 6.2(b), 6.4(b) [2] shows  $\Delta C_H$  for [Peak<sup>#1</sup> + Peak<sup>#2</sup>] and only

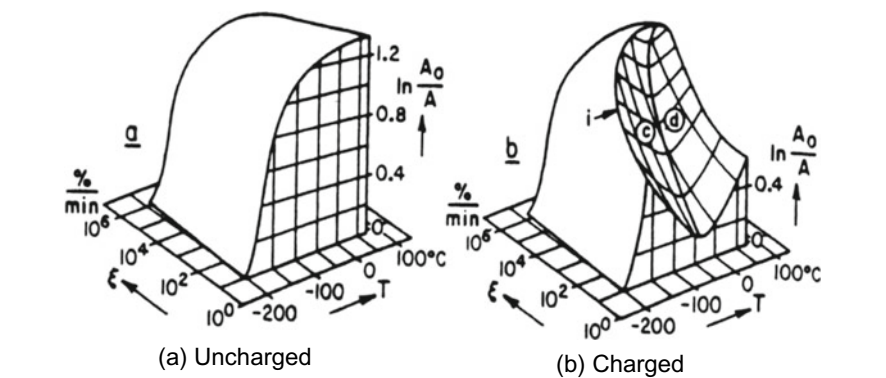


**Fig. 6.3** Schematic diagram for effects of strain rate and temperature on tensile properties of mild steel with and without hydrogen (Bernstein [3]. Reprinted with permission from TMS)

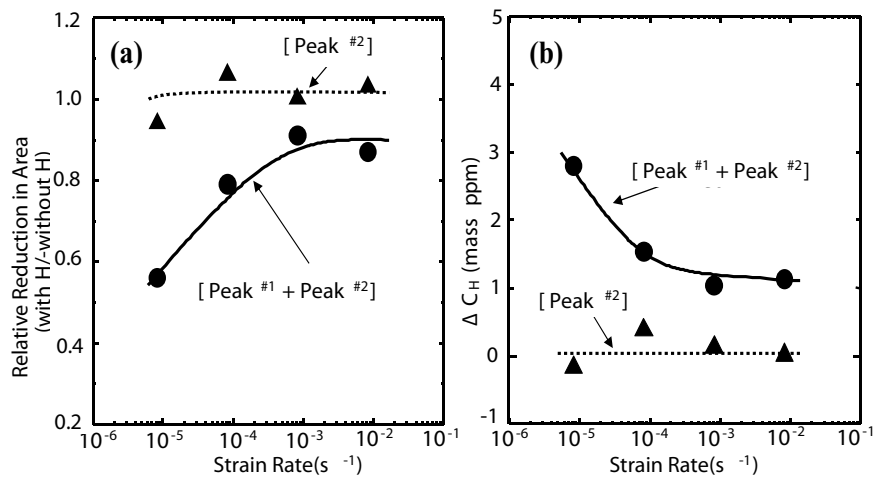


**Fig. 6.4** Strain-rate dependencies of (a) relative reduction in area at tensile tests for specimens containing [Peak $^{\#1}$  + Peak $^{\#2}$ ] hydrogen and only [Peak $^{\#2}$ ] hydrogen, (b) difference of Peak $^{\#1}$  hydrogen,  $\Delta C_H$ , between specimens strained to 0.08 with and without hydrogen for [Peak $^{\#1}$  + Peak $^{\#2}$ ] and [Peak $^{\#2}$ ] series (Doshida et al. [2])

[Peak $^{\#2}$ ] specimens at different strain rates. The  $\Delta C_H$  for the [Peak $^{\#1}$  + Peak $^{\#2}$ ] series increased at lower strain rates, but it was immune to strain rates for the [Peak $^{\#2}$ ] series. The results correspond well to the degradation of tensile ductility shown in Fig. 6.4(a). Hydrogen effects are relevant to the enhanced creation of strain-induced defects composing Peak $^{\#1}$ , and the strain-rate dependence of degradation is associated with the amount of strain-induced defects. The strain-rate dependence is also shown in Figs. 7.23 and 7.24 in Sect. 7.4.2 for the effects of cyclic prestressing.

Similar experiments were conducted for the temperature dependence of tensile ductility. The hydrogen-enhanced loss of ductility appeared significantly with increasing test temperatures from 223 to 348 K for specimens containing Peak<sup>#1</sup> hydrogen, while the ductility of specimens containing only Peak<sup>#2</sup> was almost immune to hydrogen. The temperature range in which the increase in  $\Delta C_H$  appeared for the [Peak<sup>#1</sup> + Peak<sup>#2</sup>] series was coincident with that for the loss of ductility. The vacancy-type entity of lattice defects relevant to the strain-induced increase in Peak<sup>#1</sup> hydrogen is described with Figs. 3.10–3.12 in Sect. 3.2.3.2 about low-temperature thermal desorption spectroscopy.

Positron annihilation spectroscopy was further successfully applied to discriminate lattice defects involved in the strain-rate effect [4, 5]. Positron lifetime in tensile-strained pure iron exhibited a long lifetime component exceeding 250 ps when hydrogen was precharged. The component corresponded to vacancy clusters, and its relative intensity increased with decreasing strain rates in accord with the behavior of  $\Delta C_H$ . It is a complementary and more direct support for the notion that the strain-rate dependence of the susceptibility to hydrogen embrittlement is closely related to the strain-induced creation of vacancies and their clusters.

### 6.1.2 Damage Generation During Straining

Discussion on the function of hydrogen in embrittlement has addressed mostly the crack initiation and growth in the late stages of deformation. *However, hydrogen in the final deformation stage is not necessarily required for the embrittlement to appear*, as demonstrated for iron and Inconel 625 alloy [6]. The experiments were organized to interpose unloading and reloading during tensile tests of hydrogen-precharged specimens, as schematically shown in Fig. 6.5 [6]. Unloading was applied during straining at about half or close to the fracture strain for iron or Inconel 625 alloy, respectively, and degassing at 303 K or annealing at 573 K was conducted at the unloaded stage.

Figure 6.6 [6] shows tensile curves of Inconel 625 subjected to the unloading and subsequent reloading, shown in Fig. 6.5. Hydrogen precharging, (b), substantially degraded tensile properties, and the interposed unloading did not affect the degradation of the hydrogen-charged specimen when reloaded immediately. (c) Removing hydrogen at the unloaded stage remained a substantial degradation despite the absence of hydrogen in the later stage. (d) On the other hand, annealing at 473 K completely recovered degradation. The result demonstrates that embrittlement is due to the strain-induced creation of vacancies enhanced by hydrogen preceding the crack initiation and growth, i.e., the HESIV mechanism described in Sect. 3.2.3.2. The effect of annealing at 473 K also rules out the degrading function of hydrogen via activating dislocations.

A matter of concern in tensile testing is the onset of necking, i.e., plastic instability during straining. Figure 6.7(a) [7] is an example of tensile stress–strain curves of Type 304 and Type 316L austenitic stainless steel at room temperature with and without

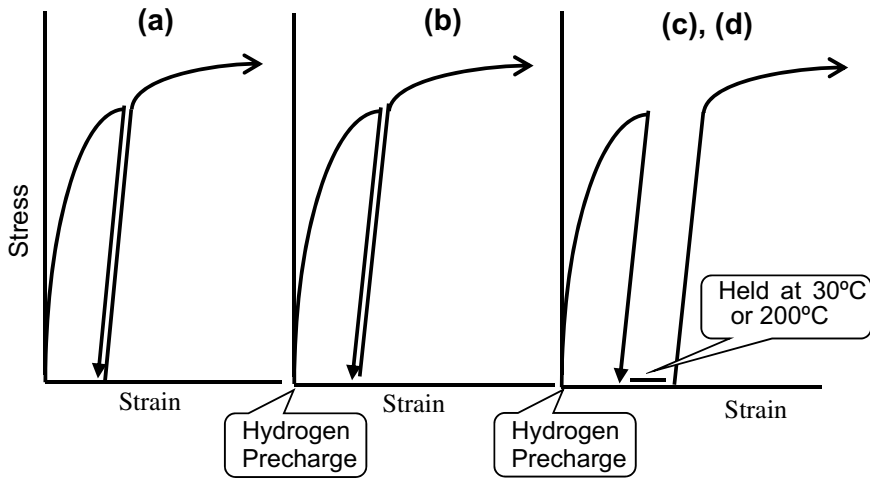
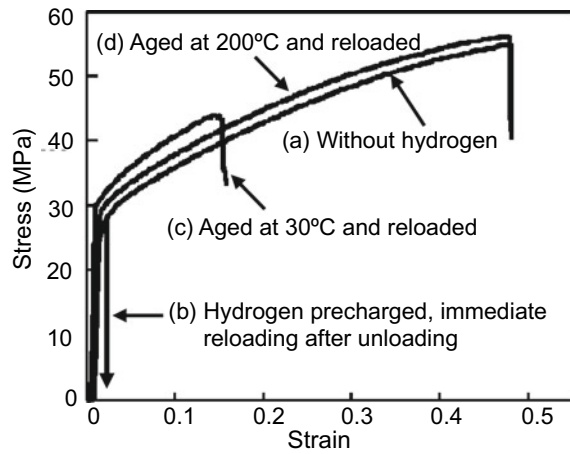


**Fig. 6.5** Procedures of interposed unloading and reloading during tensile test. **(a)** Immediate reloading after unloading without hydrogen precharging. **(b)** Hydrogen precharged and immediate reloading after unloading. **(c)** Hydrogen precharged and aged at 30 °C (303 K) or **(d)** at 200 °C (473 K) after unloading (Takai et al. [6])

**Fig. 6.6** Stress–strain curves of Inconel 625 at tensile tests with interposed unloading shown in Fig. 6.5 (Takai et al. [6])



hydrogen precharging. Hydrogen was uniformly precharged in 10 MPa hydrogen gas at 673 K to about 35 mass ppm. Hydrogen degradation appeared in Type 304 steel, and the onset of fracture was apparently discontinuous in the uniform elongation stage. It was like the onset of brittle fracture triggered by the nucleation of an incipient crack.

However, a careful examination of the stress–strain curve revealed a rather continuous load drop, as shown in Fig. 6.7(b). Since the strain rate was as low as  $8.3 \times 10^{-4}/s$ , an elongation of 0.5% spent about 1 min. The finding suggests that hydrogen promoted the onset of plastic instability. Still, the diffusion of hydrogen is not likely

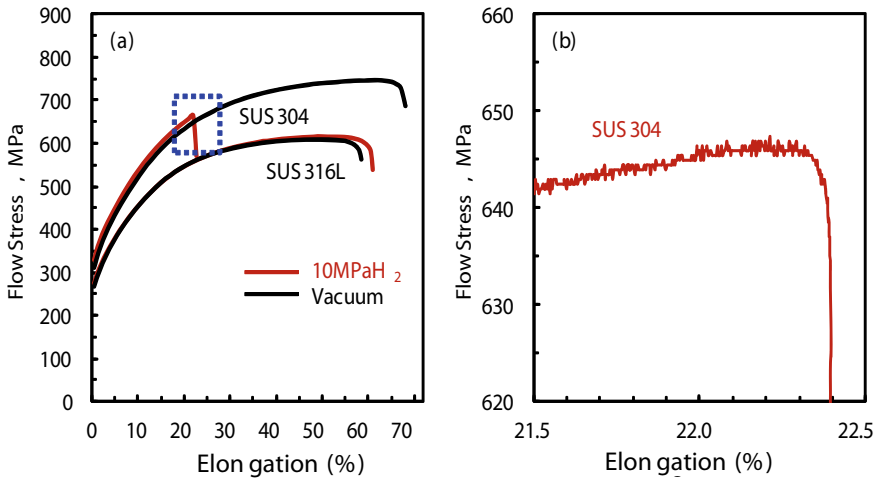


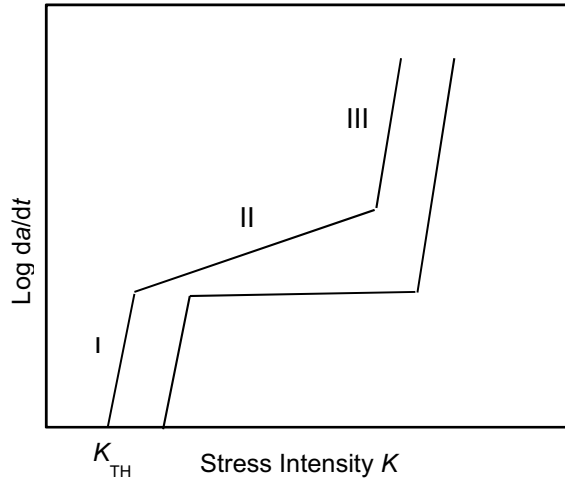
**Fig. 6.7** (a) Stress–strain curves of Type 304 and Type 316L stainless steels with/without hydrogen precharging. (b) A magnified view of the curve near the load drop of hydrogen-charged Type 304 (Hatano et al. [7])

the cause of the instability since diffusion of hydrogen in austenitic stainless steels is almost negligible during the test at room temperature. The mechanism of the early onset of plastic instability is not definite, but the decrease in stress-carrying capacity due to increasing lattice disorder is feasible. Related descriptions of the event are in Sect. 7.3.3 about plastic instability and in Sect. 8.3.4 (b) about strain localization.

## 6.2 Fracture Mechanics Tests

The fracture toughness of materials is evaluated by various test methods using notched or precracked specimens. Charpy impact tests are not appropriate for assessing hydrogen embrittlement because of involved high strain rates. Fracture toughness is expressed in terms of various quantities such as stress intensity factor ( $K$ ), crack-opening displacement (COD), and  $J$ -integral [8, 9]. The macroscopic crack initiates at the notch root or the precrack tip. The initiation and slow growth rates of cracks are schematically shown in Fig. 6.8 as a function of applied  $K$ . Below a threshold stress intensity  $K_{TH}$ , crack growth is negligible, and  $K_{TH}$  is usually denoted as  $K_{ISCC}$  for stress corrosion cracking under plane strain conditions. Crack growth rates generally exhibit three stages. The growth rate in Stage II is much lower than in Stage I or insensitive to  $K$ . Stage III corresponds to the final fracture when  $K$  reaches the fracture toughness  $K_c$  of the material.  $K$  increases with the crack growth under sustained-load testing at constant applied stress. On the other hand, in constant displacement loading using wedge-opening load (WOL) compact tension (CT) specimen,  $K$  decreases with the crack growth. Another threshold stress intensity is  $K_{th}$

**Fig. 6.8** Schematic diagram of three stages of slow crack growth rates with increasing stress intensity



for crack arrest, the value at which the crack growth ceases. Fracture mechanics tests usually employ bulky specimens, and the inhomogeneous distribution of hydrogen makes difficult the exact estimation of the hydrogen concentration at active sites for fracture in the specimen.

## 6.2.1 Crack Initiation

### 6.2.1.1 Stress Intensity Factor Approach

The initiation and growth of a crack are detected using fatigue-precracked WOL, CT, and double cantilever beam (DCB) specimens under controlled environments [10–14]. Data of  $K_{TH}$  in hydrogen gas were compiled by Moody and Robinson, as shown in Fig. 6.9 [15] for AISI steel of different yield strengths. The  $K_{TH}$  values strongly depend on the yield strength and decrease to some limiting values with elevated hydrogen gas pressure. An observed relationship between  $K_{TH}$  and  $P_{H_2}$  at room temperature for AISI 4340 steel of 1240 MPa in yield strength was [10].

$$K_{TH} = 151 - 60 \log P_{H_2} \quad (15 < P_{H_2} < 115), \quad (6.1)$$

where the unit of  $P_{H_2}$  was 6.89 kPa ( $= 10^{-3}$  ksi) and the unit of  $K_{TH}$  was  $1.1 \text{ MPa} \cdot \text{m}^{1/2}$  ( $= 1 \text{ ksi} \cdot \text{in}^{1/2}$ ). However, a lower limit existed for  $K_{TH}$  at high hydrogen gas pressures above 690 kPa. The pressure dependence of  $K_{TH}$  is strongly dependent on the yield stress of steel, and the dependence is also sensitive to the  $K_{TH}$ 's magnitude.



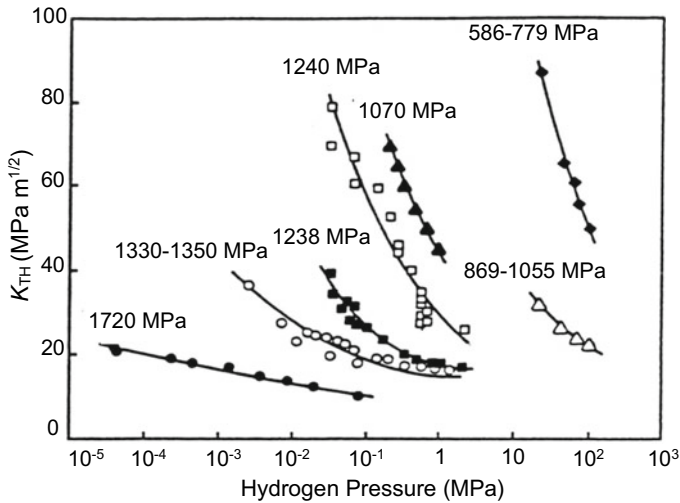


**Fig. 6.9** Effects of hydrogen pressure on the threshold stress intensity  $K_{TH}$  for crack initiation for AISI 4340 steel of various yield strengths (in MPa) (Moody et al. [15])

$K_{TH}$  increases with rising temperature [10, 15]. Low  $K_{TH}$  values at room temperature are similar to Fig. 6.3 for tensile ductility. The dependence differs by steel and the magnitudes of  $K_{TH}$ . An Arrhenius relationship that indicates a thermally activated process for the same steel as used for Eq. (6.1) in 551 kPa hydrogen was [10],

$$K_{TH} = 3631 \exp\left(-\frac{1471}{T}\right) \quad (6.2)$$

$298 < T(K) < 480$ ,

where the unit of  $K_{TH}$  was  $1.1 \text{ MPa} \cdot \text{m}^{1/2}$ .

$K_{TH}$  decreases with the increasing strength of steel at a given hydrogen gas pressure. The yield strengths of the steel, shown in Fig. 6.9, were controlled through microstructural alterations by varying tempering temperatures. Microplasticity at the crack front should play a role in the degradation, but the intrinsic factor or microscopic process that controls such dependencies is not simple.

Takeda and McMahon determined  $K_{TH}$  or  $K_{ISCC}$  values in modified WOL tests from the stationary load value that was reached after decreasing with time from a load drop on step loading [16]. In measurements for a 5% Ni HY 130 steel in hydrogen gas, Takeda et al. noticed that a subtle crack initiation occurred along the periphery of plastic hinge or slip lines well below the detectable  $K_{TH}$  on loading [16]. Takeda et al. discussed concerns of impurity segregation in grain boundaries, and related descriptions concerning impurity effects are in Sects. 7.2.4 and 8.1.4 (a).

### 6.2.1.2 *J*-Integral Approach

The validity of the stress intensity factor as a parameter of the stress and strain fields in front of the crack has limitations when crack-tip plasticity extends. COD and *J*-integral are then employed to properly evaluate fracture toughness for medium strength steels. The *J*-integral is a path-independent integral along an arbitrary counterclockwise path  $\Gamma$  around the crack tip, and it is defined as

$$J = \int_{\Gamma} \left( w dy - T_i \frac{\partial u_i}{\partial x} ds \right), \quad (6.3)$$

where  $w$  is the strain energy density,  $T_i$  is the  $i$ -th component of the traction vector,  $u_i$  is the  $i$ -th component of the displacement vector, and  $ds$  is the length increment along the contour  $\Gamma$ . *J*-integral is a measure of the energy dissipated per unit length of crack tip for per unit distance of the crack advance. *J*-integral is experimentally obtained from the specimen geometries and the load versus load-point displacement curve area.

The *J*-integral value at the onset of stable crack growth,  $J_{TC}$ , is determined as the intersection of the crack blunting line with the *J* versus  $\Delta a$  curve.  $J_{TC}$  is denoted as  $J_{IC}$  for pure mode I loading, as shown in Fig. 6.10 [17]. In many practical situations, multiple loading modes superpose, and mode III loading causes localized shear ahead of the crack tip. An empirical correlation was proposed to relate the mixed-mode fracture toughness with the process zone size [18].

Hydrogen effects on mixed mode I/III fracture toughness were examined for high-purity Ni–Cr–Mo–V steel of tempered lower bainitic structure and 855 MPa tensile strength [17]. Hydrogen was precharged in a 13.8 MPa hydrogen gas environment at 373 K to a hydrogen concentration of 2 at. ppm, equivalent to a hydrogen fugacity of 1.26 GPa at room temperature. In order to adjust the shear stress component,

**Fig. 6.10** Typical mode I *J*-resistant curve for a pure mode I test (Gordon et al. [17])

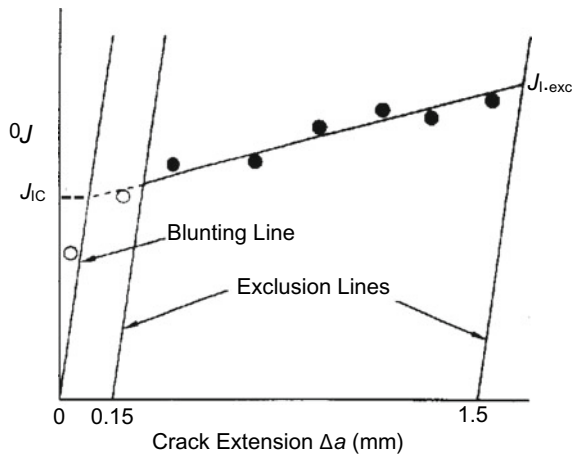
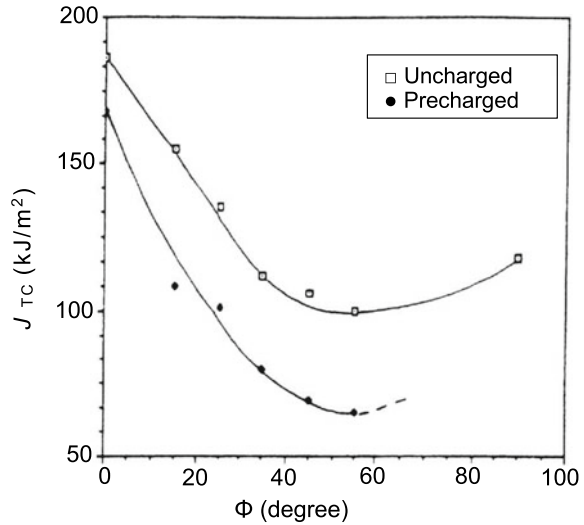


**Fig. 6.11** A plot of  $J_{TC}$  versus tilting angle  $\Phi$  showing  $J_{TC}$  decreasing with increasing mode III loading (Gordon et al. [17])



CT specimens with a slant notch of varied angle  $\Phi$  were used. Figure 6.11 [17] shows that the increasing mode III component, i.e., increasing  $\Phi$ , decreases  $J_{TC}$  in both hydrogen-charged and uncharged conditions and that hydrogen additionally enhances the degradation by about 30%. The fracture surface exhibited smaller and more uniform dimples associated with increasing the mode III loading component. The findings imply that plasticity plays a role in crack initiation and that *hydrogen is incorporated in the degradation through plasticity*. The mechanistic explanation of the finding is described in Sect. 10.4 concerning the autocatalytic void formation model for the mechanism of HE.

Experimental determination of the crack initiation from the precrack is often not precise in medium-strength steel. A method for detecting the onset of stable crack growth from the precrack tip was devised [19] by recording the progress of crack-tip opening displacement  $\delta$ , according to the theory by Needleman and Tvergaard [20] described in Sect. 10.1.2.1. The onset of the stable crack growth expects a discontinuous increase in  $\delta$ , accompanying a jog to appear on the  $\delta$  versus  $J$ -integral curve. However, the jog will be too small to be directly detected. Alternatively, the gradient of the curve is more sensitive to the appearance of a jog, as schematically shown in Fig. 6.12.

The method was applied to a three-point bending test of notched specimens of low-carbon steel of 450 MPa tensile strength. The result is shown in Fig. 6.13(a) [21], in which the yield strength  $\sigma_y$  normalizes  $J$ -integral. The maximum on the  $\delta/(J/\sigma_y)$  versus  $J/\sigma_y$  curve corresponds to the evolution of a jog on the  $\delta$  versus  $J/\sigma_y$  curve. A simultaneous measurement of electric resistance across the ligament in front of the precrack confirmed the crack initiation, as also shown in the figure. The crack initiation points detected by the two methods were entirely consistent. The result

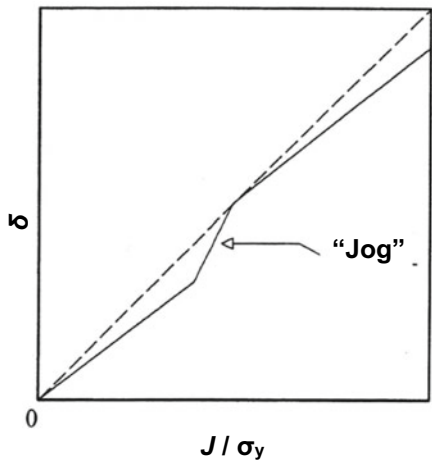


**Fig. 6.12** Schematic illustration of the appearance of a “jog” on crack opening displacement  $\delta$  versus  $J$ -integral normalized by yield stress

well reproduced a previous result for low-carbon low-alloyed steel of 600 MPa in tensile strength [19].

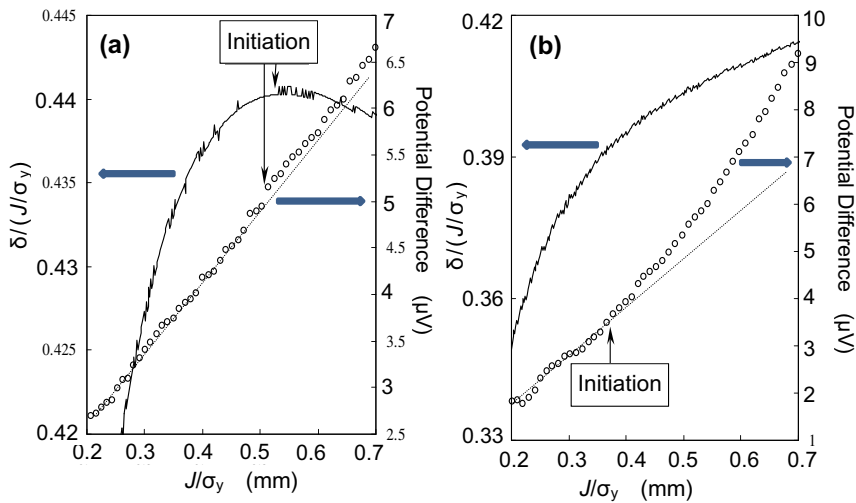


**Fig. 6.13** Ratio of crack opening displacement,  $\delta$ , to  $J/\sigma_y$  versus increasing  $J/\sigma_y$  at a three-point bending test of notched specimen of a low-carbon steel. Concurrently observed electric potential drop across the notch is also shown. (a) Without and (b) with hydrogen precharging (Shimomura et al. [21])

Subsequently, the above method was applied to hydrogen effects on crack initiation. The same steel used for Fig. 6.13(a) was hydrogen precharged to 0.82 mass ppm under a relatively mild fugacity, using cathodic electrolysis in an aqueous solution of 3% NaCl + 3 g/l NH<sub>4</sub>SCN at a current density of 5 A/m<sup>2</sup> for 24 h. A promoted crack initiation by hydrogen was revealed using the electric resistance method, as shown in Fig. 6.13(b), but  $\delta/(J/\sigma_y)$  increased continuously with  $J/\sigma_y$  without showing a maximum. It implies that the opening of the precrack proceeds gradually without a large step-wise advance. The theory by Needleman and Tvergaard [20], in Sect. 10.1.2.1, assumed that a discontinuous advance of the crack at a critical amount of void volume fraction is caused by the loss of stress-carrying capacity in the area adjacent to the crack. The observed gradual growth suggests that hydrogen, coupled with strain-induced defects, progressively reduces the stress-carrying capacity.

## 6.2.2 Crack Growth

### 6.2.2.1 Growth Rate—Gaseous Hydrogen Environment

The crack growth rate is directly measured [12, 13] or is calculated from the time record of the compliance of the specimen [10, 14]. Crack growth kinetics varies with the strength level, hydrogen concentration, and temperature. Crack growth rate is important for kinetics of hydrogen embrittlement, and it has been examined mostly for Stage II in the three stages shown in Fig. 6.8. The steady crack growth rate at Stage II is little affected by the magnitude of stress intensity and is likely rate-controlled by some factors other than the mechanical driving force.

The temperature dependence of the crack growth rate gives information on the controlling process. Temperature dependencies of the growth rate of AISI 4130 steel in 98 kPa hydrogen gas and at applied stress of 39 MPa m<sup>1/2</sup> are opposite in sign according to temperature regions as shown in Fig. 6.14 [22]. Activation energies obtained from each Arrhenius relationship were 16 and – 23 kJ/mol in Region 3 and Region 1, respectively. Similar opposite temperature dependence of Stage II crack growth rate was observed in 133 kPa dry hydrogen gas for AISI 4340 steel of 2082 MPa in tensile strength [12]. The activation energy of the Stage II crack growth in Region 3 was 14.7 kJ/mol, close to 16 kJ/mol for AISI 4130 steel.

The crack growth in dry hydrogen gas proceeds with the adsorption and following migration of hydrogen on the specimen surface. Williams and Nelson ascribed the rate-controlling process of the crack growth to the adsorption of hydrogen on the steel surface, taking into account the fractional coverage of initial adsorption sites [22]. Simmons et al. noticed that fractographic features at tests in hydrogen gas and water are similar and deduced that surface reactions of water with steel controlled the crack growth rate in water [12].

The temperature dependence of Stage II crack growth rate varies by microstructures. For experiments with 18Ni maraging steel, tensile strength levels were controlled to 1330 MPa and 1720 MPa by tempering at 473 K and 523 K, respectively

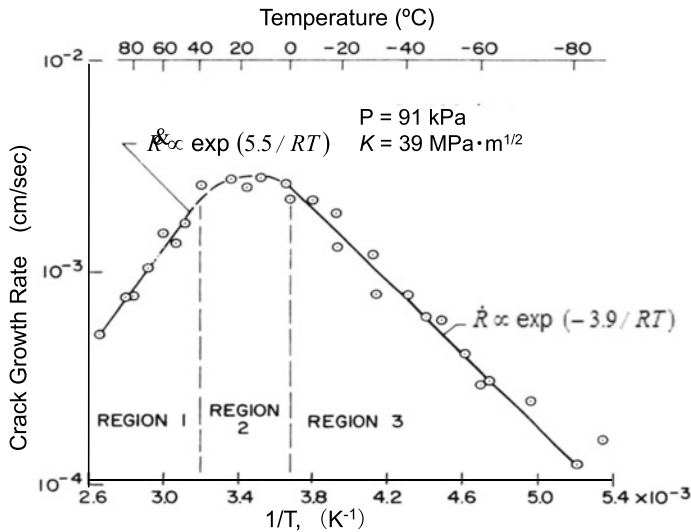


**Fig. 6.14** Temperature dependence of the crack growth rate for AISI 4130 steel in low-pressure hydrogen gas (Williams et al. [22])

[23]. The temperature dependence of Stage II crack growth rate in dry hydrogen was similar to Fig. 6.14, but the slope in Region 1 was very steep.

The transition from Region 1 to Region 3 in 133 kPa hydrogen gas occurred at about 293 K and 253 K for steels tempered at 523 K and 473 K, respectively. The crack growth rate magnitudes at the transition temperature were also substantially different between the two steels, about  $5 \times 10^{-5}$  m/s and  $5 \times 10^{-6}$  m/s for tempering at 523 K and at 473 K, respectively. The crack growth rate increased proportionately to  $\sqrt{P_{H_2}}$  in Region 3 with the activation energy of 18.4 kJ/mol, irrespective of tempering temperatures and hydrogen gas pressures. Gangloff and Wei suggested that some reactions in a near-surface region operated associated with hydrogen transport by diffusion, but the process controlling Region 1 was not definite [23].

Vehoff and Rothe found that the crack-tip opening angle (CTOA)  $\alpha$  is constant during the stable crack growth at tensile loading of notched Fe-2.6%Si single crystals in low-pressure hydrogen gas [24]. The value of  $\alpha$  characterizes ductility accompanying crack growth. The fracture surface showed a fine mixture of plastic shearing off and cleavage-like facets on a scale of 0.1  $\mu\text{m}$  or less. The value of  $\alpha$  was a function of temperature, hydrogen pressure or activities, and crack growth rate. The temperature dependence of  $\alpha$  in the intermediate temperature range, 293 K  $< T <$  390 K, showed an Arrhenius-type relation with an apparent activation energy of 49 kJ/mol. Vehoff and Rothe deduced that isolated microcracks initiated along the crack front. Related to embrittlement, Vehoff and Rothe also deduced the fractional hydrogen coverage of special sites, right at the tip of a stressed crack, with the binding energy of 49 kJ/mol [24].

Low cycle fatigue of nickel single crystals showed similar results in electrolytes at different cathodic potentials. The fracture mode was a mixture of alternate slip and local brittle fracture [25]. The apparent binding energy obtained from the temperature dependence of CTOA was 32 kJ/mol.

### 6.2.2.2 Crack Growth Rate—Internal Hydrogen

The crack growth in gaseous hydrogen likely involves surface reactions, but internal hydrogen effects have also been considered. Three stages of the crack growth rate of the type, shown in Fig. 6.8 appeared at sustained-loading tests of hydrogen precharged AISI 4340 steel [13, 26]. Hydrogen precharging was by cathodic electrolysis in a poisoned 5% H<sub>2</sub>SO<sub>4</sub> aqueous solution at a current density of 20 A/m<sup>2</sup>, and hydrogen was enclosed within the specimens by cadmium plating [26]. The crack growth in hydrogen-precharged specimens exhibited an incubation time and a transient stage before establishing the steady-state Stage II. The growth rate at room temperature was at least one order of magnitude faster for specimens of 1620 MPa yield strength tempered at 503 K than for 1340 MPa specimens tempered at 723 K. Stage II crack growth rates also depended on temperature with Arrhenius relations.

A theoretical model for the crack growth rate assumed the build-up of local hydrogen concentration to a critical value in the crack tip region by diffusion, triggering fracture there and inducing the crack advance [26]. Using numerical values of parameters obtained from the literature, experiments, and adjusting as a variable, the calculated crack growth rates fitted pretty well with the observed temperature dependence for 503 K tempering. The estimated binding energies of hydrogen with the critical trap sites for the crack initiation were 75 kJ/mol and 27 kJ/mol for 503 K and 723 K tempering, respectively. Fractographic features were mixtures of inter-granular (IG) and quasi-cleavage (QC) for specimens tempered at 503 K. For tempering at 723 K, alternate IG and MVC regions were assigned to intermittent slow and fast crack growth. Details of fractographic features are described in Sect. 7.2.4.

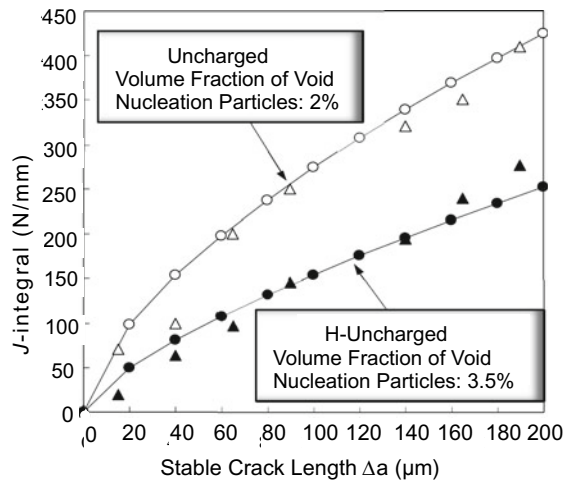
In the model proposed by Gerberich et al. [26], crucial assumptions are (1) the fracture stress decreasing in proportion to hydrogen concentration and (2) high local hydrogen concentrations due to both the dilatational stress field and trap-binding effects. The plastic constraint was also considered for computing the triaxial stress at the critical site. The critical trap sites to cause sequential fracture were assigned from fractographic observations to martensite lath boundaries intersecting the prior austenite grain boundaries for 503 K tempering and to oxysulfides located at the edge of plastic zone for tempering at 723 K. However, the critical hydrogen concentrations that the model estimated at the trap sites were very high, more than 10<sup>6</sup> times of hydrogen in solution. The crack growth is further described in Sect. 8.1.1 about changes of fractographic features and Sect. 9.3.2 about the mechanism.

### 6.2.2.3 Crack Growth Resistance

The  $J$ -integral is a measure of energy dissipation associated with crack advance, and the crack growth resistance curve ( $R$ -curve) is the plot of  $J$  value versus crack extension ( $\Delta a$ ) in slow stable crack growth. The  $R$ -curve reflects internal changes causing the energy dissipation during the crack advance. A previous study for low-carbon ferrite–pearlite steel demonstrated a noticeable decline in the  $R$ -curve by increased strain-induced lattice defects, presumably vacancies [27]. In the experiment, lattice defects were detected using thermal desorption analysis (TDA) of hydrogen introduced as a tracer of lattice defects, described in Sect. 3.1.1.3. A simulation of the  $R$ -curve using a constitutive relation for porous material and a finite element method (FEM) calculation showed that an enhanced void generation reduces the crack growth resistance [28].

The simulation method was applied to the effect of hydrogen on the  $R$ -curve. Figure 6.15 [29] compares  $R$ -curves of notched specimens of low-carbon ferrite–pearlite steel subjected to three-point bending tests with and without hydrogen precharging. Hydrogen charging was conducted in a mild condition by cathodic electrolysis in a 3% NaCl + 3 g/l  $\text{NH}_4\text{SCN}$  aqueous solution at a current density of 5 A/m<sup>2</sup> for 24 h. A substantial decrease in the crack growth resistance appeared in hydrogen-charged specimens. The  $\Delta$  and  $\blacktriangle$  marks in the figure denote specimens without and with hydrogen precharging, respectively, and  $J$ -integral values are calculated from the stress and strain fields near the crack. In the simulation, the volume fractions of the void nucleating particle,  $f_N$ , were adjusted from experimentally determined 2% for the hydrogen-free material to 3.5% for the hydrogen-charged material, to make a good fit to the observed  $R$ -curves.  $f_N$  for the hydrogen-free specimen was for a specimen given plastic strain just before the maximum stress. Accordingly, the decrease in the  $J$ -integral by hydrogen was ascribed to an increase in nucleation void

**Fig. 6.15**  $R$ -curves of low-carbon ferrite–pearlite steel with and without hydrogen precharging.  $\circ$ ,  $\bullet$ : Observed values,  $\Delta$ ,  $\blacktriangle$ : Calculated values using a finite element method (Nagumo et al. [29])





densities. Details of the modeling method for the  $R$ -curve in Fig. 6.15 are described in Sect. 10.1.2.3.

Effects of hydrogen on  $R$ -curve were also shown for disk-shaped compact tension specimens of 21Cr–6Ni–9Mn austenitic stainless steel [30]. Hydrogen was thermally precharged to 210–230 mass ppm in high-pressure hydrogen gas. The fracture initiation toughness  $J_Q$  was defined as the  $J$  value at the intersection of the 0.2 mm offset blunting line with the  $R$ -curve. Alternatively, initial damage at the precrack-tip was detected as a subtle deviation from the linearity of the COD versus crack length measurement using the direct current potential difference according to ASTM E1737. The deviation point was denoted as  $J_i$  and  $J_Q$  according to the choice of the initial blunting line. Hydrogen reduced  $J_i$  and  $J_Q$  by more than 80% of the values for hydrogen-free specimens. Crack growth resistance denoted by  $dJ/da$  also decreased nearly 50% by hydrogen. Nibur et al. carefully examined deformation microstructures exhibiting enhanced strain localization and deduced that any mechanism that hydrogen directly lowers fracture resistance was not feasible [30]. Surface morphologies of strain localization are described in Sect. 7.4.1.1.

The  $R$ -curve is strongly dependent on the microstructures of steels. For ferrite–pearlite steels, carbides precipitated along grain boundaries act as barriers against slip extension across grain boundaries and affect  $R$ -curves prominently [27]. The functions of the slip constraint in  $R$ -curve are described in Sect. 10.1.2.3, concerning the strain-induced creation of vacancies.

## 6.3 Fatigue

Fatigue failure is the most common failure of metallic structural components in practical services. Not only in high-pressure hydrogen gas environments, but hydrogen also comes from humid or corrosive environments, during cathodic protection of off-shore structures, or at electroplating. Hydrogen produced by corrosion reactions on the metal surface is often a cause of corrosion fatigue failure.

Fatigue properties of materials are commonly expressed in terms of fatigue life and fatigue limit, determined by plotting the stress amplitude versus the number of cycles to failure ( $S$ – $N$  curve). The fatigue limit  $\Delta\sigma_c$  and the threshold stress intensity range for no detectable crack growth  $\Delta K_{th}$  are design parameters for the safety against fatigue failure [31]. Fatigue failure proceeds through the crack nucleation and growth. Measurements of fatigue-crack growth in laboratories are conducted commonly using notched specimens. Fatigue tests consume a substantial time for one run, and hydrogen contents in specimens are often not constant during a test-run due to the entry and loss of hydrogen and/or internal changes of materials.

Fatigue failure is affected by many factors; their effects are not similar among different expressions of fatigue properties. Gerberich reviewed early works for hydrogen effects on metal fatigue concerning different approaches such as total life, crack threshold, and growth [32].

6.3.1 Fatigue Limit

Hydrogen generally reduces fatigue life and fatigue limit. Figure 6.16 [33] plots tension–compression fatigue test data of two lots of surface-hardened 0.36C–Cr–Mo martensitic steel with/without hydrogen. Hydrogen was initially charged by immersing specimens in a 20% NH<sub>4</sub>SCN aqueous solution at 323 K, and hydrogen contents were controlled to 10, 0.8, and 0.3 mass ppm by partial degassing at room temperature. Fatigue specimens contained a small hole of 100 μm in diameter and depth on the specimen surface as the crack starter. Fatigue tests were conducted at a stress ratio  $R$  ( $= \sigma_{\min}/\sigma_{\max}$ ) of  $-1$  and with different frequencies up to 1000 Hz. Hydrogen was recharged to specimens every  $8 \times 10^6$  fatigue cycles to keep the same content during the test. The control of hydrogen content was by partial degassing, and the reductions in fatigue life and fatigue limit by hydrogen were reversible against the entry of hydrogen. A small amount,  $\sim 0.3$  mass ppm, of hydrogen existed in as-heat-treated specimens, and thermal desorption analysis (TDA) showed a small peak at 573 K, indicating a strongly trapped non-diffusive nature of residual hydrogen as described in Sect. 2.1.2.

On the other hand, artificially charged hydrogen diffused out at room temperature, and the thermal desorption ceased by 573 K. The observations imply that diffusive hydrogen causes degradation. Murakami et al. revealed the fatigue-crack initiation from non-metallic inclusions [33]. Non-metallic inclusions are viable trap sites of non-diffusive hydrogen, but non-diffusive hydrogen is generally immune to degradation. Alternatively, diffusive hydrogen might interact with non-metallic inclusions

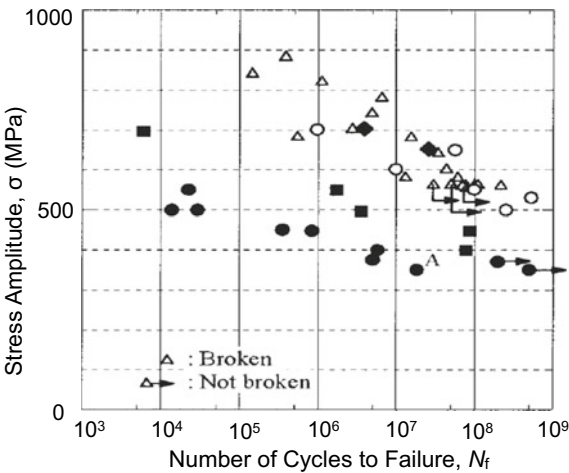


**Fig. 6.16** Effects of hydrogen on  $S$ – $N$  diagram of two lots of SCN 435 steel. Open marks: as-heat-treated (0.3 ppm H), solid marks: H-charged. Initial hydrogen contents are controlled by partially degassing at room temperature after hydrogen charging: ● (10 ppm), ■ (100 h after hydrogen charging, 0.8 ppm), ♦ (4300 h after hydrogen charging, 0.3 ppm) (Murakami et al. [33])



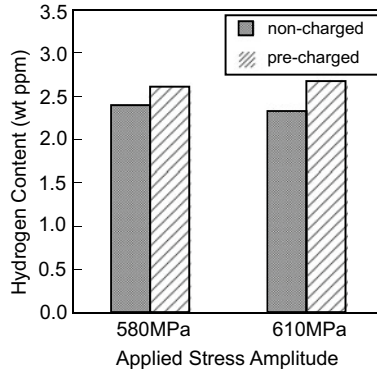


**Fig. 6.18** Amounts of tracer-hydrogen in Si–Cr steel specimens fatigue-fractured at two applied stress amplitudes with and without hydrogen precharging. Fatigue cycles applied to the non-charged and precharged specimens were respectively  $6 \times 10^6$  and  $5.5 \times 10^6$  at the stress amplitude of 580 MPa, and  $2 \times 10^5$  and  $8 \times 10^4$  at the stress amplitude of 610 MPa (Nagumo et al. [34])

cracks existed at the ends of the surface notch in both air and hydrogen atmospheres. Ogawa et al. confirmed that the short fatigue cracks were non-propagating, i.e., the fatigue limit was a non-propagation limit of small cracks [36].

### 6.3.2 Crack Initiation and Growth-Rate Near Threshold

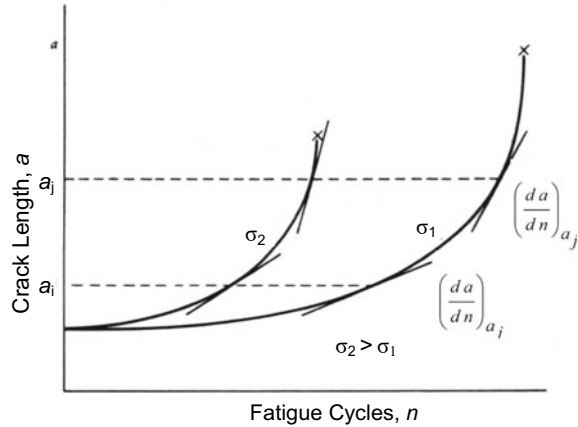
The kinetics of the fatigue crack growth commonly uses the stress intensity range  $\Delta K$  as a parameter.  $\Delta K$  is defined as

$$\Delta K = K_{\max} - K_{\min}, \quad (6.4)$$

where  $K_{\max}$  and  $K_{\min}$  are the maximum and the minimum stress intensity factor per cycle.  $\Delta K$  at which the crack growth initiates is defined as the threshold stress intensity range,  $\Delta K_{\text{th}}$ . Accurate detection of the crack initiation and then of  $\Delta K_{\text{th}}$  is difficult. Reported hydrogen effects on  $\Delta K_{\text{th}}$  differ, increased or decreased, by steel types and environments [37].

The growth of a fatigue crack starting from the surface notch is schematically shown in Fig. 6.19 [31] against fatigue cycles for two applied stresses. The crack growth rate is computed from the observed crack length record. However, precise crack growth rate measurements are problematic in a regime as low as  $1 \times 10^{-9}$  m/cycle, and the computed growth rate does not necessarily mean the step-by-step-crack advance. In this case, a measured crack growth rate denotes the number of cycles needed for the crack to advance a certain distance feasibly in a step. Environments often complicate the morphology of the notch root, and effects of corrosion or oxidation overlap hydrogen embrittlement.

**Fig. 6.19** Schematic illustration of applied stress dependence of fatigue crack growth (Hertzberg [31])



Environmental effects on fatigue crack growth of high-strength steels are complicated according to  $\Delta K$  levels and stress ratios. Accelerated fatigue crack growth in hydrogen gas compared to that in the air was reported for 2.25Cr–1Mo steel at two growth rate regimes, i.e., at near threshold levels and at higher growth rates, typically  $> 10^{-8}$  m/cycle above a critical  $K_{\max}$  value [38]. The hydrogen effect in the latter regime appeared at frequencies below a critical value (e.g., 5 Hz at the stress ratio of 0.05), associated with a fracture mode change to predominately intergranular cracking, consistent as a general strain-rate effect in hydrogen embrittlement.

On the other hand, near the threshold levels below  $10^{-9}$  m/cycle, the accelerated growth rate in dry hydrogen compared to moist air appeared only at low load ratios [38]. Suresh et al. ascribed the influence of the environment on the near-threshold fatigue crack growth to the oxide-induced crack closure mechanism. An earlier contact between the fracture surfaces during the closure portion raises the closure load and reduces  $\Delta K_{\text{eff}}$  as,

$$\Delta K_{\text{eff}} = K_{\max} - K_{\text{cl}}, \quad (6.5)$$

where  $K_{\text{cl}}$  is the stress intensity at which the crack surface contact occurs. The reduced  $\Delta K_{\text{eff}}$  decelerates crack growth rates at low load ratios. The deceleration of the crack growth due to the crack closure is prominent when the crack opening is small at low  $\Delta K$  levels and low stress ratios in corrosive environments. The magnitude of the mechanical wedging action is a function of the thickness and location of the debris [39]. Suresh et al. noted that pulsating crack-tip opening displacements were of a size comparable to fracture surface roughness and the thickness of corrosion debris within the crack [38].

The initiation and the early-stage growth of fatigue crack, especially in the range of very small  $\Delta K$  under corrosive environments, have been extensively studied [32, 40]. Fatigue crack growth rates of high-strength steel under the same applied stress intensity increased in 3% NaCl aqueous solution and water compared to those in air.

The increase was much higher for short than long cracks [32]. An expression of short crack effects is to use  $\Delta K_{\text{eff}}$  by adding an effective crack length  $l_0$  to the actual crack length  $l$  [40, 41], i.e.,

$$\Delta K_{\text{eff}} = A \Delta \sigma \sqrt{\pi(l + l_0)}, \quad (6.6)$$

where  $A$  is the elastic stress concentration factor, and  $\Delta \sigma$  is the applied nominal stress range. The magnitude of  $\Delta K_{\text{eff}}$  is larger than the apparent  $\Delta K$ , and the contribution of  $l_0$  to  $\Delta K_{\text{eff}}$  is significant when  $l$  is small. Environmental effects are ascribed to large  $l_0$  in the presence of a corrosive environment. However, the physical meaning of  $l_0$  is not definite, while an intrinsic defect size such as a microfracture process zone size has been proposed.

Hydrogen enhancement of the fatigue crack growth rate at the near-threshold region was deduced by Esaklul et al., separating crack closure effects [42]. The steel was AISI 4340 of 1800 MPa in the tensile strength, and hydrogen was precharged under a pretty high fugacity by cathodic electrolysis in poisoned 5%  $\text{H}_2\text{SO}_4$  at a current density of 20 A/m<sup>2</sup> followed by cadmium plating. Fatigue tests were conducted using compact tension (CT) specimens at  $R = 0.1$  and 30 Hz. Log  $da/dN$  versus nominal  $\Delta K$  showed a hydrogen enhancement of the crack growth rates at  $\Delta K$  above 7 MPa-m<sup>1/2</sup> or in  $da/dN$  above  $5 \times 10^{-9}$  m/cycle. However, in the lower  $\Delta K$  range, crack growth rates were almost identical for hydrogen-charged and uncharged specimens. Fractographic features showed oxide buildup and geometrical asperities for hydrogen-charged specimens, and the load versus the crack-opening-displacement curves exhibited closure of the crack surface. Then, the nominal  $\Delta K$  was converted to  $\Delta K_{\text{eff}}$  in Eq. (6.5), using the estimated contact area and contact point on the observed fracture surface. Then, the modified plot of log  $da/dN$  against  $\Delta K_{\text{eff}}$  revealed hydrogen-enhanced crack growth rates even in the  $\Delta K_{\text{eff}}$  range below 5 MPa-m<sup>1/2</sup> or in  $da/dN$  below  $1 \times 10^{-9}$  m/cycle.

### 6.3.3 Stage II Crack Growth in Steel

#### 6.3.3.1 Effects of Microstructures

The dependence of the fatigue crack growth (FCG) rate on increasing  $\Delta K$  is schematically similar to Fig. 5.6 in creep and Fig. 6.8 in fracture mechanics tests. The FCG rate in Stage II is commonly expressed by Paris' law as,

$$\frac{da}{dN} = A \Delta K^m, \quad (6.7)$$

where  $A$  and  $m$  are constants that vary with material, environment, and testing conditions [31, 37]. Paris' law is originally an empirical relation, and the measured  $m$ -values are 3–4 for various metallic materials.

An early study showed increased crack growth rates with increasing hydrogen gas pressure [43]. Figure 6.20 shows FCG of high-strength 0.4C–Ni–Cr–Mo martensitic steel (SNCM 435 in Japanese Standard) subjected to three types of heat-treatment to different microstructures and tensile strengths, i.e., annealed at 1123 K (991 MPa), as-quenched (1344 MPa), and quenched-tempered (1274 MPa). The specimens were a double cantilever beam (DCB) type. Fatigue tests were in hydrogen gas environments of 1.1 and 4.0 MPa at the stress ratio  $R = 0.1$  and a sinusoidal test frequency of 5 Hz. The growth rates at a given  $\Delta K$  were in the order of the tensile strength. The transition from Stage I to Stage II was not discernible, and  $m$ -values applying Paris' law in hydrogen environments were substantially higher than conventional values of 3–4, as observed in Ar. The  $m$ -value was also higher for the tempered martensite than for the annealed or as-quenched ones, as shown in Table 6.1 [43].

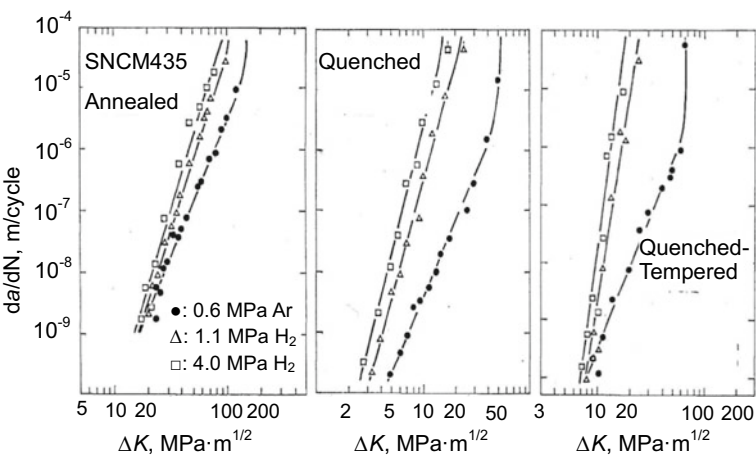


**Fig. 6.20** Fatigue crack growth rates in high-pressure Ar and H<sub>2</sub> of high-strength martensitic steel subjected to three different heat treatments. The stress ratio is 0.1, and the test frequency is 5 Hz (Fukuyama et al. [43]. Reprinted with permission from The Soc. Mater. Sci., Japan)

**Table 6.1** Fatigue crack growth parameter  $m$  in Eq. (6.7) for 0.4C–Ni–Cr–Mo steels in Ar and hydrogen environments

Steel	Annealed			Quenched (TS:1344 MPa)			Quenched-Tempered (TS: 1274 MPa)		
	Ar	1.1 MPa H <sub>2</sub>	4 MPa H <sub>2</sub>	Ar	1.1 MPa H <sub>2</sub>	4 MPa H <sub>2</sub>	Ar	1.1 MPa H <sub>2</sub>	4 MPa H <sub>2</sub>
$m$	4.2	6	6.3	4.1	6.5	7.1	4.7	12.1	15.6
$K_Q$ (MPa $m^{1/2}$ )	163	111	99	59	23	17	72	27	21

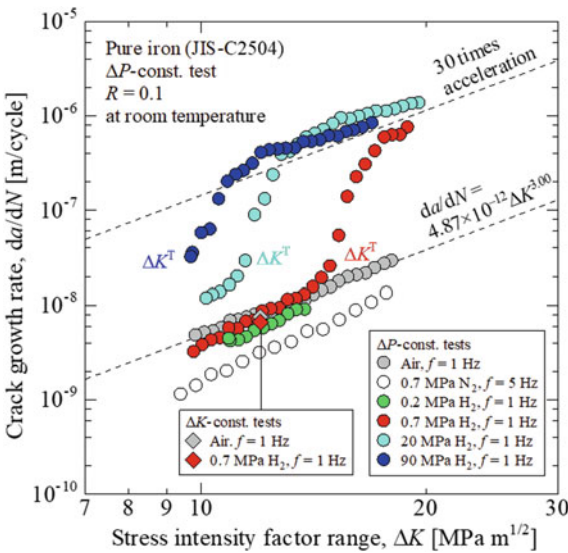
Fukuyama et al. [43]. Reprinted with permission from The Society of Materials Science, Japan

In experiments by Fukuyama et al., the threshold  $\Delta K_{th}$  was not definite, but hydrogen substantially accelerated FCG for the as-quenched specimens even at low  $\Delta K$  near the threshold, suggesting a decrease in  $\Delta K_{th}$ . On the other hand, the FCG rates of annealed or tempered specimens were almost immune to hydrogen in the small  $\Delta K$  range. The reason for the difference between the two steels is not definite, but the stability of dislocation configurations might be a feasible one. Closure effects due to oxides or debris are not likely since all the tests were conducted in dry environments. The susceptibility to hydrogen embrittlement in terms of fracture toughness  $K_Q$  is included in Table 6.1, and the reductions by hydrogen, in terms of the ratio to the fracture toughness in Ar gas, were of similar levels for the two heat treatments.

Precise measurements of FCG in high-pressure hydrogen gas environments have been extensively conducted in recent years. Ogawa et al. measured the FCG rate for pure iron in 0.2–90 MPa hydrogen gas [44]. Figure 6.21 compares the FCG curves with those in the air and 0.7 MPa nitrogen gas. The constant load-amplitude ( $= \Delta P$  constant) fatigue tests were conducted using CT-type specimens at the load ratio  $R$  ( $= P_{min}/P_{max}$ ) of 0.1 and a test frequency of 1 Hz. In the air and 0.7 MPa nitrogen, the FCG curves were linear with  $m$ -values of nearly 3.0. On the other hand, the FCG rate in hydrogen gas increased during Stage II to about 30 times higher than in air or nitrogen gas.

The onset of hydrogen acceleration, or the transition, occurred in the intermediate  $\Delta K$  range, and the higher hydrogen gas pressure promoted the start of acceleration. A noticeable fact was that the onset of acceleration was during Stage II, i.e., after a significant stable crack growth, in a relatively low-pressure hydrogen gas. It suggests that substantial activation of plasticity is the precursor for hydrogen acceleration. It is

**Fig. 6.21** Fatigue crack growth rates of pure iron in laboratory air and high-pressure nitrogen and hydrogen (Ogawa et al. [44])



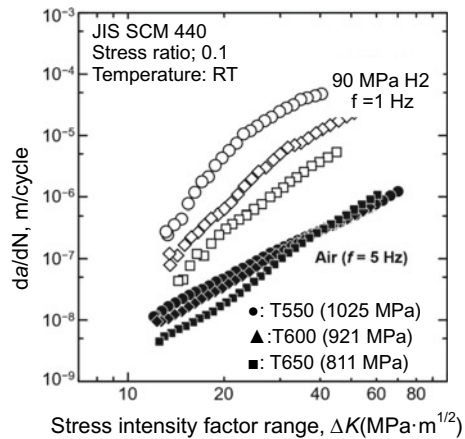


also to be noticed that hydrogen gas pressure hardly affected the later FCG rate after acceleration. During the transitional acceleration stage before attaining a new steady crack growth, the fraction of intergranular (IG) fracture morphology decreased, as shown in Fig. 7.10 in Sect. 7.2.6.

Similar transitions by hydrogen in Stage II FCG rate appeared for ferrite–pearlite [45, 46], and martensitic [47] steels. In ferrite–pearlite steel, increasing carbon contents, i.e., the pearlite volume fraction, raised  $\Delta K$  to start the transition [46]. After reaching the higher Stage II ( $m \sim 3.63$ ), tentatively termed as Stage II', the FCG rates in 0.7 MPa hydrogen were about 15, 13, and 5 times the values in air, for 0.16, 0.25, and 0.55% C steels, respectively. Pearlite mitigates hydrogen-assisted fatigue crack acceleration.

Hydrogen acceleration of FCG is much remarkable in martensitic steel. Figure 6.22 shows FCG curves for 0.4C–Cr–Mo martensitic steels prepared to different tensile strengths of 1025, 921, and 811 MPa by varying tempering temperatures [47]. The fatigue tests using CT specimens were conducted in air or 90 MPa hydrogen gas at the stress ratio  $R$  of 0.1 and test frequencies of 5 or 1 Hz. Acceleration of the FCG rates in 90–115 MPa hydrogen sharply appeared when the steel's tensile strength exceeded 900 MPa, particularly at low test frequencies or strain rates. The FCG rates at  $\Delta K$  of  $30 \text{ MPa}\cdot\text{m}^{1/2}$  in a  $\Delta K$ -constant fatigue test were 100–2000 times the values in the air. Another notable feature in Fig. 6.22, compared to Fig. 6.21 for pure iron, is a wide transition range of  $\Delta K$  and an uncertain finish to Stage II'. Large  $m$ -values obtained in Fig. 6.20 might correspond to the transition from Stage II to Stage II'. Concerning substantially different FCG rates near Stage II' among the three steels, differences in the original martensite microstructures are to be noticed. The FCG rate in Stage II' in the hydrogen environment is the higher for higher strength or lower tempering temperature.

**Fig. 6.22** Fatigue crack growth rates in laboratory air and high-pressure hydrogen gas of high-strength steel prepared to different tensile strength by tempering temperatures (Setoyama et al. [47])



### 6.3.3.2 Effects of Test Conditions

Hydrogen embrittlement is generally more prominent in higher hydrogen concentrations, and temperature and strain rate play in the extent of degradation, as described in Sect. 6.1.1 on tensile tests. In fatigue tests under hydrogen gas environments, the effects of hydrogen also depend on testing conditions.

#### (a) Temperature

In the FCG test of ferrite–pearlite steel in 0.7 MPa hydrogen gas, Yamabe et al. showed the start of the FCG rate acceleration to delay with increasing temperature from room temperature to 363 K and 423 K [45]. The attained steady Stage II' growth rates also decreased associated with the temperature rise. A similar dependence of the start of the FCG rate transition was exhibited for pure iron, raising the temperature from 298 to 373 K, and 423 K in 0.7, 10, and 90 MPa hydrogen gas [48]. Such results likely correspond to the case of tensile tests shown in Fig. 6.3. Effects of temperature on Stage II' growth, after reaching a new steady state, were not sure in pure iron. Acceleration by hydrogen did not occur at  $\Delta K$  less than 14 MPa·m<sup>1/2</sup> at 423 K in pure iron, even in 90 MPa hydrogen gas which expected a high hydrogen concentration. On the other hand, in low-carbon ferrite–pearlite steel, acceleration of the FCG rate occurred even at 423 K in 0.7 and 10 MPa hydrogen gas environments [49].

#### (b) Test frequency

A strong dependence of FCG on the test frequency was demonstrated for high hardness SAE 52100 bearing steel (Vickers hardness number 569) [50]. The wedge-opening-load (WOL) specimens were hydrogen-precharged in 100 MPa hydrogen gas at 358 K (~ 1.5 ppm). The fatigue test was under a constant load range at the load ratio  $R = 0.1$ , and test frequencies were 0.2, 2, and 20 Hz. The FCG rates steeply increased at  $\Delta K$  of about 6 MPa·m<sup>1/2</sup>, inclining to the initial Stage II growth line. The test frequencies hardly affected the steep increase, but the FCG rates in the newly attained Stage II' were remarkably higher with decreasing strain rates. Any difference in the  $m$ -values by test frequencies was not sure.

FCG tests in high-pressure hydrogen gas also exhibited the dependence of the FCG rate on test frequency. Sun et al. cyclically changed the test frequency during the fatigue test of 15–5 PH martensitic stainless steel in 0.9 MPa hydrogen gas [51]. A decrease in the frequency from 20 to 0.2 Hz during a certain number of fatigue cycles induced a significant enhancement of the FCG rates. After the crack propagated over a predefined distance at 0.2 Hz, returning the frequency to 20 Hz decreased the crack growth rate, recovering the values under 0.9 MPa at a frequency of 20 Hz. The enhanced FCG rate by the lower frequency was associated with intergranular fracture (IG) surface.

For ferrite–pearlite steel, a substantial acceleration occurred on decreasing the test frequencies as low as 0.01 Hz in 90 MPa hydrogen gas [46]. For martensitic steels of different strengths, 811, 921, and 1025 MPa in tensile strength, a wide range of the test frequencies from 1 to 0.001 Hz exhibited strong dependencies of the FCG rate on frequencies [47]. In that case, a step-wise frequency change was

conducted at  $\Delta K$  of 30 MPa·m<sup>1/2</sup>. At 0.001 Hz, the FCG rate was as much as 2500 times the value in the air for the 921 MPa steel. On the other hand, for the 811 MPa steel, hydrogen acceleration was about 20–30 times in the air, almost immune to the frequency change.

The fracture surface of steel of 921 and 1025 MPa in tensile strength contained a few tens % of IG surface. However, the fraction of the IG surface was almost unaffected by the test frequency, suggesting that the fraction of the IG surface was not necessarily the essential origin of the acceleration. Lower frequencies need a longer time per cycle, extending hydrogen entry at the crack tip.

### (c) Environmental impurity effect

As described in Sect. 6.3.2 oxide-induced crack closure is a factor to be considered in the near-threshold regime for enhanced crack growth rates in hydrogen gas. Somerday et al. examined the inhibiting function of oxygen in the onset of hydrogen acceleration in Stage II FCG [52]. The constant load-amplitude fatigue tests were conducted using CT specimens of API X52 steel at the stress ratio  $R$  of 0.1 or 0.5 and a test frequency of 10 Hz. The environments were 21 MPa pure hydrogen or (H<sub>2</sub> + O<sub>2</sub>) mixture of up to 1000 vol. ppm O<sub>2</sub>. Hydrogen-accelerated fatigue crack growth was activated when exceeding both threshold levels of the inert environment crack growth rate and  $K_{\max}$ . The  $\Delta K$  at the onset of accelerated crack growth systematically increased as oxygen enriches in hydrogen gas. Either a lower load cycle frequency or a higher  $R$  ratio delayed the onset of hydrogen-accelerated crack growth to higher  $\Delta K$  levels.

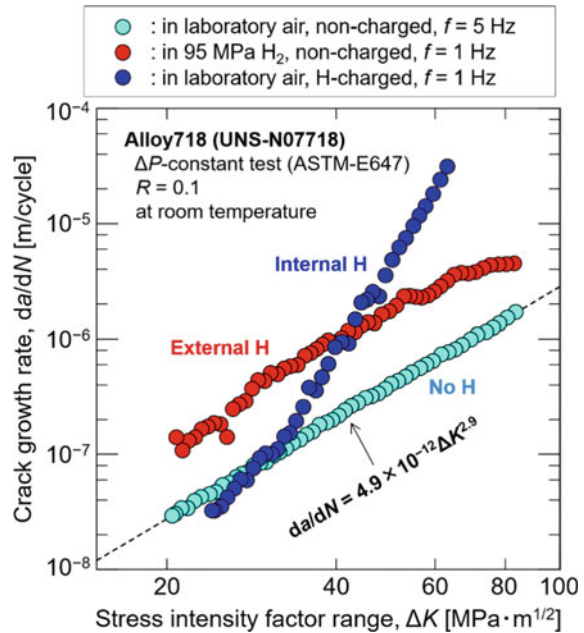
About the function of oxygen, Somerday et al. assumed that the crack tip coverage by oxygen, disturbing hydrogen entry into the matrix, is overcome when the rate of new crack tip surface creation reaches a critical level. Once this condition is attained, hydrogen uptake at the crack tip is enhanced and hydrogen-accelerated fatigue crack growth can proceed [52]. Accordingly, a balance between oxygen transport to the crack tip and the creation rate of the new crack surface determines the onset of hydrogen acceleration of FCG. The steady stage II' FCG rates after acceleration were reasonably irrelevant to oxygen contents, suggesting hydrogen–matrix interactions are unaffected.

### (d) Internal hydrogen

In the experiment on an environmental effect cited above [52], the hydrogen supply from the environment is a crucial process for the FCG rate. Ogawa et al. compared FCG of a hydrogen-precharged Ni-base superalloy 718 (internal hydrogen) with that in high-pressure hydrogen gas [53]. The alloy was a face-centered cubic (FCC) structure, precipitation-hardened with  $\gamma'$  (Ni<sub>3</sub>(AlTi)) and  $\gamma''$  (Ni<sub>3</sub>Nb). Hydrogen precharging was likely uniform by exposing specimens to 100 MPa hydrogen gas at 543 K for 600–800 h. Fatigue tests using CT specimens were under a constant load range at the load ratio  $R = 0.1$  and a test frequency of 1 Hz. The hydrogen gas pressure for tests of uncharged specimens was 95 MPa.

Figure 6.23 shows FCG curves under external and internal hydrogen conditions [53]. Under the external hydrogen condition, the FCG rate was 3–6 times faster than that in air, with the same  $m$ -value of nearly 3 in Paris' law. On the other hand, the FCG

**Fig. 6.23** Fatigue crack growth rates of Alloy 718 in high-pressure hydrogen gas (External H) compared with hydrogen-precharged (Internal H) one (Ogawa et al. [53])



rate under the internal hydrogen condition steeply increased with increasing  $\Delta K$ , far exceeding values under the external hydrogen condition. Separately conducted measurements of the frequency dependence of FCG exhibited a monotonic increase in the FCG rates with decreasing test frequencies at  $\Delta K$  of 50 MPa $\cdot$ m $^{1/2}$  under both external and internal hydrogen conditions. However, in all frequencies, no hydrogen acceleration appeared at a low  $\Delta K$  of 30 MPa $\cdot$ m $^{1/2}$  under the internal hydrogen condition.

Fractographic features exhibited intergranular and quasi-cleavage surfaces under the external hydrogen condition, while fine planar facets appeared under the internal hydrogen condition. Fractographic features characterizing hydrogen embrittlement are described in Sect. 7.2.5. The origin of the difference between external and internal hydrogen is not definite. However, be noticed is that tolerations of hydrogen effects in a cyclically stressed volume element in front of the advancing crack are more frequent under the internal hydrogen condition than the external one.

### 6.3.4 Fatigue in Austenitic Stainless Steel

Austenitic stainless steel is characterized by low hydrogen diffusivities and occasional phase instabilities. Murakami et al. measured the FCG from a surface notch on Type 304 and 316L stainless steels containing 24–90 mass ppm hydrogen [54]. The specimens were round bars of 7 mm in diameter, and hydrogen was precharged at

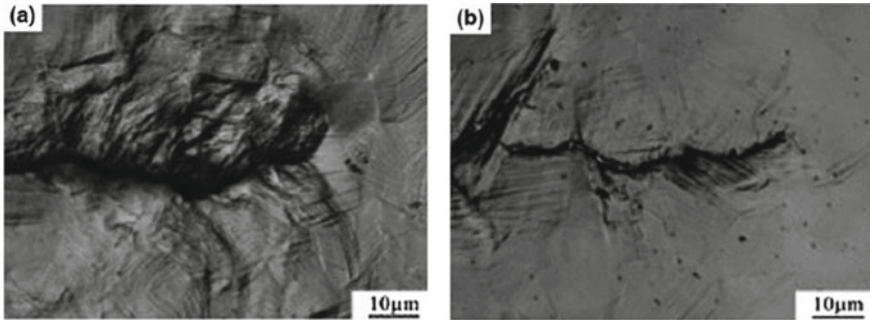


**Fig. 6.24** Slip deformation behaviors near fatigue crack front in Type 304. (a) Uncharged,  $N = 13,200$ , (b) hydrogen-charged to 47.2 mass ppm,  $N = 18,400$  (Murakami et al. [54])

~ 553 K in high-pressure hydrogen. A small hole, 100  $\mu\text{m}$  in both depth and diameter, was drilled on the surface after hydrogen charging as the starter of a fatigue crack. A tension–compression fatigue test with a constant-stress amplitude of 280 MPa was conducted at 1 Hz and a stress ratio of  $-1$ , and the advancing crack length was measured on the surface using a replica method.

Hydrogen generally promotes crack initiation and growth in fatigue, but an unexpected “decrease” was found in the FCG rates in both types of stainless steel. The decrease was significant for Type 304 with high hydrogen concentrations of  $\geq 70$  mass ppm. The surface relief around the crack is due to plastic deformation, and hydrogen precharging much reduced the relief, as shown in Fig. 6.24 [54]. Murakami et al. deduced that, at a high hydrogen concentration, material surrounding a crack blocked the extension of the plastic zone at the crack tip. Internal hydrogen builds up a dilatational stress field, and hydrogen desorption associated with the crack extension, when it occurs, will release the stress field, reducing plastic deformation around the extending crack.

Hydrogen degradation in 45 MPa hydrogen gas was negligible or very small for Type 316L stainless steel in tensile tests, the stress–fatigue life diagram at tension–compression tests, and the FCG tests [55]. Type 316L was immune also to fatigue tests using cyclic pressurization of tubular specimens by 88 MPa hydrogen gas [56]. The cycle time was 20 s per cycle. On the other hand, similar tests showed a substantial decrease in the fatigue life for Type 304 and precipitation-hardened A286 steels. Microscopic observations revealed crack paths along the interfaces of  $\alpha'$  martensite in Type 304 and  $\text{Ni}_3\text{Ti}$  in A286.

Hydrogen effects on microstructural alterations during fatigue tests are prominent in Type 304 [57]. Characteristics of hydrogen embrittlement of austenitic steel are in Sect. 8.3.

### 6.3.5 High-Cycle Fatigue Near Threshold

Fatigue crack growth behaviors near the threshold stress intensity range are of practical importance for structural components under long-term service. The threshold  $\Delta K_{th}$  is  $\Delta K$  below which the crack growth rate becomes diminishingly small.  $\Delta K_{th}$  was not definite in ultrasonic tension–compression fatigue tests of mild steel, Type 304 stainless steel, and copper in a 3.5% NaCl aqueous solution, while a clear threshold existed in non-corrosive silicon oil [58]. The fracture morphology of samples given fatigue cycles in a corrosive environment changed from ductile transgranular to intergranular fracture.

The involvement of a minimal amount of hydrogen in extremely high-cycle fatigue limits was presented by Murakami et al. [59] for surface-hardened Cr–Mo steel quenched and tempered in a reductive atmosphere (QT) or in a vacuum (VQ). Hydrogen entered into specimens during the fabrication process to concentrations of 0.7–0.9 and 0.01 mass ppm for QT and VQ, respectively. Fatigue tests were tension–compression at  $R = -1$  with cyclic frequency of 20–80 Hz. For extremely high-cycle fatigue in the regime of  $N > 10^7$ , the  $S$ – $N$  plots showed a substantial scatter, but fatigue lives and the fatigue limit were lower for QT than VQ.

Murakami et al. pointed out the importance of non-metallic inclusions for  $\Delta K_{th}$  [59]. Subsurface non-metallic inclusions located at centers of fish-eye were crack initiation sites, associated with an optically dark area (ODA) characterized by rough and irregular surface morphology. ODA in QT was about twice as large as that of non-metallic inclusions and was larger than ODA in VQ. Secondary ion mass spectroscopy detected hydrogen at near non-metallic inclusions in QT but not in VQ. Murakami et al. deduced that hydrogen assists the formation of ODA and determines fatigue lives at low stress levels near the fatigue limit [59]. At an extremely slow crack growth stage of  $1 \times 10^{-10}$  m/cycle, a detectable crack advance needed more than thousands of cycles. Effects of some structural damages might be expected.

### 6.3.6 Models of Fatigue Crack Extension

Paris' law in Eq. 6.7 for the FCG was originally derived for the fatigue-life prediction in designing metallic construction. Hydrogen acceleration of FCG rate appears in coefficient  $A$  in Eq. 6.7, with an exponent  $m$ -value common to many metals, but transition or occasionally large  $m$ -values appear, as described in preceding sections. To understand the function of hydrogen in fatigue, microscopic origins of such parameters are indispensable knowledge. However, the issue is not yet conclusive. Details of the discussion made so far are beyond the scope of this book, and brief outlines of the main ideas are as follows.

### 6.3.6.1 Criteria for the Crack Advance

Paris' law is originally an empirical one to give the best fit with  $m = 4$  [60, 61], and its theoretical derivations followed concerning criteria for the fatigue crack advance. Preceding Paris' law, Head proposed a stress-controlled advance for a relatively short rack [62]. Head considered three types of neighboring volume elements in the crack front, tolerating work hardening, plastic constraint, and shear, differing by their sites. The widths of the respective elements are determined by the force balance under a boundary condition. Assuming that the crack advance occurs when work hardening exceeds the fracture stress of the material, Head derived the crack growth rate proportional to  $K^2$ .

In the small-scale yielding condition, the crack opening displacement (COD)  $\delta$  more correctly expresses stress fields ahead of the crack. Donahue et al. assumed the crack growth rate to increase proportionately to the difference from a critical value, as [63]

$$\frac{da}{dN} = A(\delta - \delta_{th}). \quad (6.8)$$

Since

$$\delta = \frac{4K^2}{\pi\sigma_y E}, \quad (6.9)$$

Equation (6.8) written in terms of  $K$  is.

$$\frac{da}{dN} = \frac{4A}{\pi\sigma_y E} (K^2 - K_{th}^2), \quad (6.10)$$

where  $A$  is a material constant,  $\sigma_y$  is the yield stress, and  $E$  is Young's modulus.

Weertman considered the displacement  $D$  of two atomic planes forming the upper and lower surface of a crack and assumed its critical value  $D^*$  as the condition of the crack advance [64]. Weertman also assumed cyclic variations of  $D$  in fatigue tests are additive and that the critical  $D^*$  is the sum of  $D$  at each cycle. Summing of cyclic  $D$  implicitly presumes accumulation of plastic work at each cycle. Weertman calculated accumulated plastic work  $W_p$  over the plastic zone. On the crack advance,  $W_p$  converts to the newly created surface energy. Giving proper expressions for the plastic zone size, Weertman derived the crack growth rate in the form of Paris' law,

$$\frac{da}{dN} = C(\Delta K)^4. \quad (6.11)$$

The coefficient  $C$  is inversely proportional to the surface energy  $\gamma$ , i.e.,  $C$  increases with decreasing  $\gamma$ .



### 6.3.6.2 Models in Respect of Damage Accumulation

Criteria of crack advance, such as  $\Delta K_{th}$  or  $\delta_{th}$ , are helpful as a design parameter for structures, but the criteria per se are not the microscopic mechanism. An approach to understanding the crack advance in fatigue is to consider the microscopic process in front of a crack leading to advance. In fatigue tests, a monotonic increase in the potential energy due to rising load is not expected, and Lee and Liebowitz remarked on internal alteration associated with plastic deformation in the crack front [65]. The energy originating in plasticity is generally irreversible on unloading, but a partial recovery occurs associated with released interactions of lattice defects with applied stress.

Bodner et al. assumed that the non-reversible work  $W_p$  stored in the plastic area around the crack tip is critical in the crack advance and proposed as [66],

$$\frac{da}{dN} = \left( \frac{da}{dW_p} \right) \left( \frac{dW_p}{dN} \right). \quad (6.12)$$

The idea implies that the elastic strain energy and accumulated lattice defects contribute to the crack advance. Kingbeil assumed that  $dW_p/da$  in fatigue is the same as the critical potential energy release rate or the fracture toughness  $G_c$  in monotonic loading [67], i.e.,

$$\frac{d\Pi}{da} = \frac{dW_p}{da} \equiv G_c. \quad (6.13)$$

During fatigue crack advance, the change in the total potential energy per cycle  $d\Pi/dN$  must balance the plastic work per cycle  $dW_p/dN$ , i.e.,

$$\frac{d\Pi}{dN} = \frac{dW_p}{dN} = \frac{dW_p}{da} \frac{da}{dN}. \quad (6.14)$$

Accordingly, from Eqs. 6.12–6.14,

$$\frac{da}{dN} = \frac{1}{G_c} \frac{dW_p}{dN}. \quad (6.14)$$

Kingbeil numerically calculated  $dW/dN$  for various metals using a finite element method and agreed well with experimental FCG curves [67]. For a titanium alloy, the calculated result was

$$\frac{dW}{dN} = 3.735 \times 10^{-8} (\Delta K)^{4.002} (J/m). \quad (6.15)$$

On the right-hand side of Eq. 6.14,  $dW_p/da$  is determined by the material's constitutive relation, while  $G_c$  concerns the degradation of materials.



The calculation of plastic energy by Kingbeil was over the entire plastic zone length. However, the plastic zone length is usually much larger than the width of one striation, which corresponds to the crack advance per cycle. A further issue is the fracture of elements within the plastic zone, and Duran et al. proposed a sequential fracture model in the plastic zone [68]. Damage generated by cyclic stressing accumulates in each volume element in the plastic zone, and its magnitude differs by the distance of the element from the crack tip. During the crack advance over the entire plastic zone, an element initially located neighboring the extent of the plastic zone tolerates cyclic damage accumulation, gradually increasing as the crack front approaches. Accumulated damage in the element when the element faces the crack tip likely attains a critical level for the crack advance.

Mechanistic models of FCG, including hydrogen effects, have not been presented. From Eq. 6.14, hydrogen effects are not likely due to the constitutive relation, like yield stress or work-hardening rate, according to findings presented in Sect. 6.1. Hydrogen feasibly operates in processes that concern degradation of the energy release rate,  $G_c$ . Damage accumulation is a viable process in fatigue. Extensive studies on fatigue in high-pressure environments are now in progress, and precise nanoscopic observations, as described in Sect. 7.3.2, will elucidate the mechanism of hydrogen effects in fatigue failure.

## 6.4 Delayed Fracture

### 6.4.1 Characterization

Eventual failure during service is a crucial problem for structural components. Molecular hydrogen precipitation is a well-established cause of delayed cracking, and modern industrial technologies, such as steel refining and welding technologies, have minimized the problem. On the other hand, delayed failure of tendons in prestressed concrete or high-strength steel fasteners under sustained loading occurs even in mildly corrosive environments. The mechanisms of these two types of delayed fracture are different, and this chapter focuses on the latter.

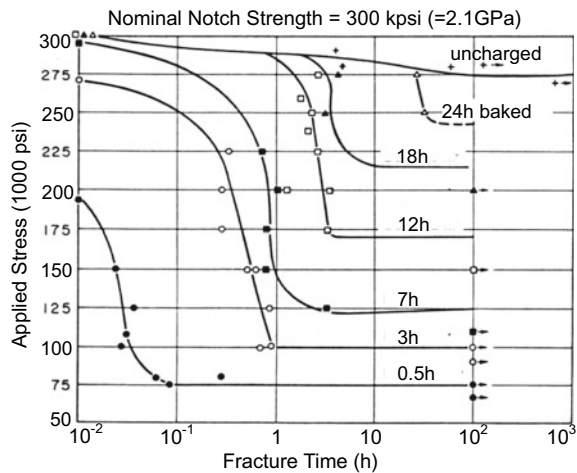
The time until failure often extends to many years. The time dependence of failure is like fatigue failure, and “static fatigue” is an alternative terminology for sustained-loading delayed fracture. The occurrence of failure depends on the environment, and delayed fracture belongs to environmental degradation of materials. Accordingly, corrosion on the surface of materials is deeply concerned with, and delayed fracture under corrosive environments is sometimes regarded as stress corrosion cracking (SCC). Hydrogen is a byproduct of corrosion reactions on the surface. When SCC dominates, corrosion pits or crevice corrosion produced by anodic dissolution on the metal surface leads to failure. On the other hand, in laboratory tests, the cathodic polarization of the specimen in liquid environments promotes failure, proving the dominant role of hydrogen in failure.

A long exposure time to fracture in engineering services inevitably necessitates some devices to accelerate failure in laboratory tests. As described in the following Sect. 6.4.2, the meaning or validity of an accelerating method is a critical issue. In laboratory tests, delayed fracture characteristics are expressed by applied stress versus time to fracture diagram similar to the  $S-N$  curve in fatigue tests. The delayed fracture diagram varies by test temperature, environment or hydrogen concentration, and specimen geometry.

Figure 6.25 by Johnson et al. [69] might be the first diagram obtained by laboratory tests under constant-stress tensile loading. The specimens of AISI 4340 steel of 1600 MPa in tensile strength were circumferentially notched bars, and hydrogen was precharged under a fairly high fugacity by cathodic electrolysis in a 4%  $H_2SO_4$  aqueous solution at a current density of 30 A/m<sup>2</sup>. Hydrogen was enclosed in specimens by cadmium-electroplating, and the specimens were then baked at 423 K to homogenize the distribution of hydrogen. Partial degassing took place during baking, but hydrogen concentrations were not measured. Instead, baking time at 423 K was the parameter of hydrogen concentration. In the experiments, as-received specimens contained about 1.5 mass ppm of hydrogen, exceeding electrolytically introduced hydrogen. The as-received hydrogen was non-diffusive and immune to embrittlement. It implies that apparent hydrogen concentrations do not always serve as a measure for causing degradation.

Figure 6.25 exhibits the incubation time to the final failure, suggesting the initiation of an incipient crack substantially prior to the final fracture. The initiation and discontinuous growth were detected using electric resistance techniques [69, 70]. Decreasing hydrogen concentration retarded the onset of the crack initiation, but the onset was almost independent of the applied stress for a given hydrogen concentration [71]. The incubation period covers most of the time to fracture at low hydrogen concentrations.

**Fig. 6.25** Delayed fracture diagram of AISI 4340 steel. Hydrogen-charged specimens are Cd-plated and baked at 423 K (150 °C) for various periods (Johnson et al. [69])



Assuming a diffusion-controlled process in the incubation period, Steigerwald et al. obtained the activation energy of 38 kJ/mol from an Arrhenius relationship for the logarithm of the ratio of the incubation time to the absolute temperature [71]. The value is fairly higher than the reported activation energies of hydrogen diffusion in iron and steel, and some other controlling processes are not ruled out.

A noteworthy result was that the true fracture stress, i.e., applied stress divided by the uncracked area measured on the fracture surface, was constant over a wide range of applied stress and hydrogen concentration. It suggests that hydrogen does not affect the fracture stress in the central portion of specimens. It was likely that hydrogen operated in some other kinetics during the incubation period, not necessarily decreasing the fracture stress at the final crack propagation stage.

Events during the incubation period of delayed fracture tests were detected using the acoustic emission (AE) technique for high-strength steel of 1300 MPa in tensile strength [72]. The delayed fracture tests used V-notched specimens subjected to a constant load cantilever bending in 0.1 N HCl solution. Acoustic emissions occurred in the incubation period prior to the onset of the crack initiation, detected by a concurrently conducted electric resistance measurement. The number of AE signals increased with time, and Fig. 6.26 compares waveforms in the incubation period and the crack growth stage [72]. The waveform in the incubation period was packet-like, similar to that associated with plastic deformation, while that in the crack growth stage was irregular with higher amplitudes. Activation of dislocations and hydrogen diffusion is certainly a process that proceeds during incubation.

Fracture mechanics test under sustained loading is a type of delayed fracture test. The threshold stress intensity for the crack initiation  $K_{TH}$ , described in Sect. 6.2.1 for fracture mechanics tests, corresponds to the lower limit of the applied stress below which delayed fracture does not occur. However, notches are not always required in specimens to induce delayed fracture. The correspondence between practical and laboratory test results is a matter that needs careful examination.

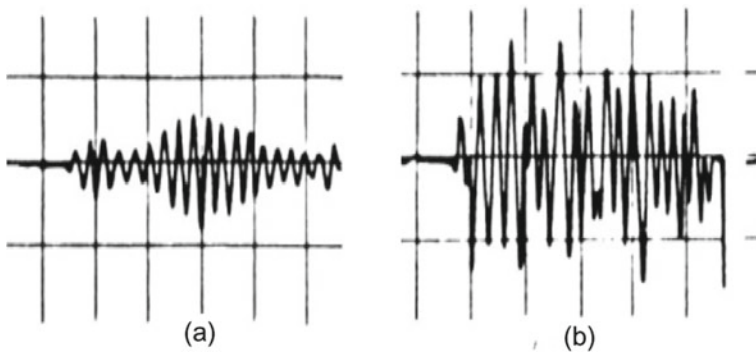


**Fig. 6.26** Wave forms of acoustic emission generated during delayed fracture tests of high-strength martensitic steel. (a) Incubation time, (b) during crack extension (Nagumo [72])

6.4.2 Effects of Materials Factors

The susceptibility to delayed fracture of steel is generally higher for higher strength levels. Figure 6.27 [73] compiles threshold stresses of various commercial steel subjected to delayed fracture tests in water for 100 h. The threshold stress turns to a decrease in steel of the tensile strength higher than 1200 MPa, which corresponds to the strength level of high-strength fasteners that exhibit delayed fracture in service under atmospheric environments. The evolution of delayed fracture on raising the strength of steel was a serious warning to industries aiming to use higher-strength steel.

A noticeable result in Fig. 6.27 is that the critical tensile strength, above which the threshold stress turns to decrease, differs by steel type. Maraging steels are more resistant to degradation than low-alloyed steels, suggesting a design principle for hydrogen-resistant steel. Testing temperature also substantially affects the time to fracture. For sustained tensile-load delayed fracture tests in water for martensitic steel of 1510 MPa in tensile strength, elevating water temperature from 298 to 353 K reduced the time to fracture to more than one order of magnitude [73]. Strengthening steel by, e.g., alloy design or heat treatment is associated with microstructural changes that alter the response to applied stress. Hydrogen interactions with strain-induced lattice defects are viable functions of hydrogen in the incubation period. Mechanistic behaviors in delayed fracture tests under sustained loading are the same as stress relaxation and creep that involve plastic deformation, described in Sect. 5.3.

**Fig. 6.27** Threshold stresses at 100 h for delayed fracture of various high-strength steels in water (Yamamoto et al. [73])

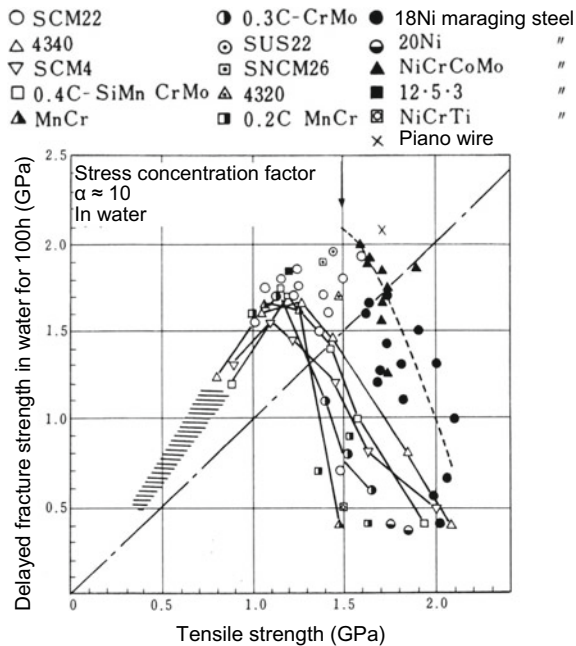
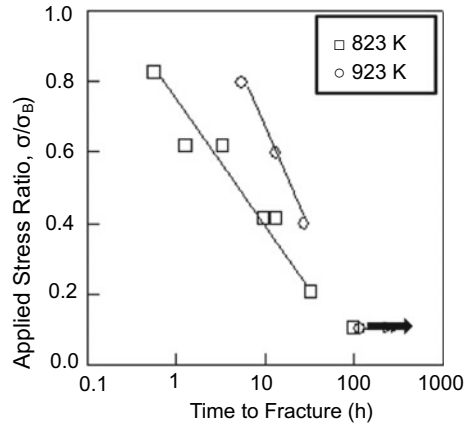


**Fig. 6.28** Delayed fracture diagrams for medium-carbon Mo-V martensitic steels tempered at 823 K (550 °C) and 923 K (650 °C). The arrow indicates unfailed specimens (Nagumo et al. [74])



Hydrogen-enhanced stress relaxation shown in Fig. 5.5 for a 0.37%C–0.6%Si–1.0%Mo–0.5%Cr–0.54 V martensitic steel indicates the precipitation of fine VC to reduce both the stress-relaxation rate and its enhancement by hydrogen. Figure 6.28 shows delayed fracture test results of the same steel in Ref. [74]. Two tempering temperatures of 823 K and 923 K were employed to give the same tensile strength of 1470 MPa with and without VC precipitation. Sustained loading tests were conducted at room temperature using a smooth hydrogen-precharged specimen. Hydrogen charging was under a mild hydrogen fugacity by cathodic electrolysis in a 3% NaCl + 3g/l<sup>-1</sup> NH<sub>4</sub>SCN solution at a current density of 5 A/m<sup>2</sup>. Precipitation of fine VC brought about a substantial improvement in the time to fracture. The correspondence between the stress-relaxation rates and hydrogen effects implies the involvement of plasticity and associated hydrogen effects in delayed fracture.

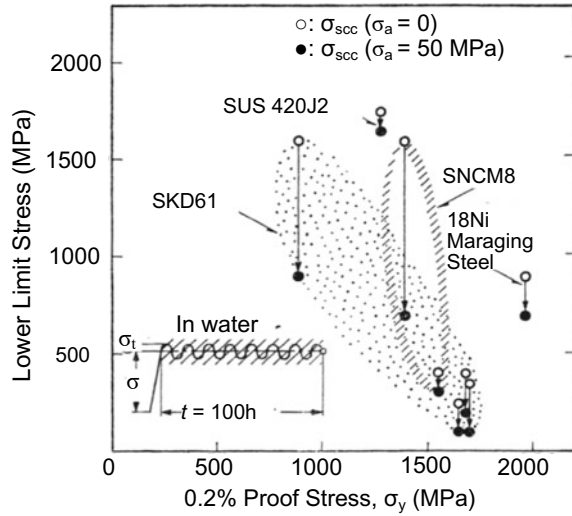
### 6.4.3 Effects of External Factors

Environmental conditions like applied stress, temperature, and humidity are not constant for structural components during engineering service. Alternating hydrogen entry due to daily humidity changes in the ambient atmosphere is demonstrated in Fig. 2.3 in Sect. 2.1.1. Delayed fracture is usually regarded as a fracture under static loading, but the effects of mechanical and electrochemical variations must be considered.

#### (a) Stress variations

The superposition of small amplitude stress oscillation on sustained loading promotes the macroscopic crack initiation and decreases the lower limit stress in delayed fracture tests [75]. The used material was a Ni–Cr–Mo steel of 1800 MPa in tensile strength, and sinusoidal oscillation of 15 or 400 cpm was superposed on U-notched static bending at various constant stresses. Promoted crack initiation by superposing

**Fig. 6.29** Decrease in the lower limit stress by superposing cyclic variations of applied stress at sustained loading delayed fracture tests for various high-strength steels (Kido et al. [76]. Reprinted with permission from The Iron and Steel Institute Japan)

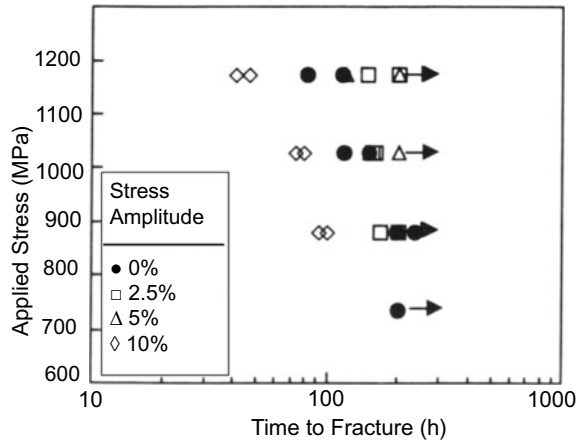


oscillating stress was prominent when dropped water at the U-notch. The degradation appeared for stress amplitude as low as 50 MPa at the constant stress of 1260 MPa, and the degradation was more prominent with higher stress amplitudes and oscillating frequencies. Results for various steels are shown in Fig. 6.29 [76] at an oscillating frequency of 15 cpm and a stress amplitude of 50 MPa. The superposed oscillating stress may induce interactive functions of hydrogen with dislocations, operating alternately in process in sustained-loading tests.

For experiments in Fig. 6.29, the maximum applied stress increased on superposing the oscillatory stress. In order to separate the effects of the cyclic variation and the applied stress level, keeping the maximum stress constant during the test was conducted [77]. During sustained-load delayed fracture tests of martensitic steel, the applied load was cyclically reduced by up to 10% at a frequency of 5 or 10 cpm [77]. The steel was 1300 MPa in tensile strength, and smooth specimens of 5 or 7 mm in diameter were immersed in a 20%  $\text{NH}_4\text{SCN}$  aqueous solution at 323 K.

Figure 6.30 [77] shows delayed fracture diagrams for various stress amplitudes. The promoted fracture was evident at a stress amplitude of 10%, while the mean stress was lower than the constant-stress level. A noteworthy finding was that the hydrogen concentration in specimens was uniquely determined by the immersion time in the solution, irrespective of constant or cyclic stressing. It implies that *total hydrogen content is not the controlling factor for promoting fracture*. The amount of lattice defects measured in terms of the amount of tracer-hydrogen introduced after the tests decreased when tested specimens were annealed at 473 K. The decrease was more significant for cyclic-stressed specimens than for sustained-loaded specimens. It indicates that cyclic activation of dislocations enhances the generation of vacancies during the incubation period. Further studies on the effects of cyclic prestressing on tensile tests and interactions between fatigue and delayed fracture are in Sect. 7.4.2 concerning damage accumulation in stress histories.

**Fig. 6.30** Accelerated fracture by superposing cyclic stress variations at delayed fracture test of high-strength steel. The maximum stress is constant (Izutsu et al. [77])



#### (b) Environmental variations

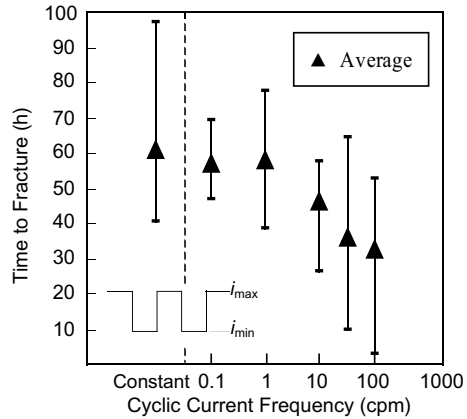
Another environmental factor to be examined is variations of hydrogen fugacity associated with weather changes. A method devised to examine the effects was to apply cyclic variations to hydrogen-charging current density [78]. Experiments used high-strength martensitic steel of 1390 MPa in tensile strength in sustained-loading tests under simultaneous hydrogen charging. The specimens were round bars of 5 mm in diameter, and mild cathodic electrolysis was conducted in a 3% NaCl + 3 g/l  $\text{NH}_4\text{SCN}$  aqueous solution. The applied tensile stress was 70% of the tensile strength, and the current density was cyclically varied from 0.1 to 100 cpm in a rectangular form keeping the maximum current density constant.

The time to fracture as a function of the frequency of the cyclic current is shown in Fig. 6.31 [78], where the maximum current density was  $7.5 \text{ A/m}^2$ , and the relative amplitude of the current variations was 10%. Promoted failure by higher frequencies is evident. The frequency of the cyclic current does not affect the total charging time, and hydrogen contents in unstressed specimens were uniquely determined by the total amount of supplied electric charge, irrespective of cyclic variations of the current density [78]. Accordingly, hydrogen content is irrelevant to the frequency effects.

Subsequent TDA analyses of trapped states of hydrogen revealed changes in TDA profiles with an elapsed time of the test. The TDA profile was a single broad peak centered at around 353 K, but the higher temperature side of the peak showed a more pronounced increase with time. Similar to the case of cyclic stress variation [77], alteration of TDA profiles with time appeared earlier for the cyclic current conditions than for the constant current test. The TDA results indicate the creation of trap sites of high binding energies. The low-temperature thermal desorption spectroscopy (LTDS), shown in Figs. 3.2 and 3.11, ascribed the origin of such TDA profiles to vacancy clustering. Effects of environmental variations are consistent with promoting vacancy clustering.



**Fig. 6.31** Effects of cyclic variation of hydrogen-charging current density on the time to fracture at delayed fracture tests of high-strength steel. The maximum current density,  $i_{\max}$ , is the same (Nagumo et al. [78])



#### 6.4.4 Laboratory Test Methods

Laboratory test methods for structural materials intend to reproduce situations in engineering practice. However, in delayed fracture, only limited information is available on the occurrence of failure in engineering service, and a long time to fracture necessitates some devices to accelerate failure in laboratories. The methods should not impede the validity of the test.

The primary purpose of mechanical tests is to evaluate the performance of materials in engineering practice. However, the term “evaluation” has two meanings; one is to assess the quality, and another is to find a numerical expression. In other words, the former is for qualification in safety and reliability, and the latter is to characterize materials. Some proposed “evaluation” methods are not necessarily definite in their purpose.

##### (a) FIP test method

A test method as a standard for prestressing steel bars for concrete was published by Fédération Internationale de la Précontraint [79]. A smooth steel bar under constant loading is immersed in a 20% aqueous solution of  $\text{NH}_4\text{SCN}$  at 323 K. The pH of the solution is 4–4.5. The title of the method was for stress corrosion cracking, and corrosion reactions were observed on the specimen surface. However, hydrogen entry of about 3 mass ppm was confirmed in high-strength martensitic steel after several hours of immersion. The time to failure is the measure of the susceptibility to cracking, but a substantial scatter of data necessitates statistical consideration. The method gives a relative measure for the quality of different steels.

##### (b) Constant load tests using hydrogen-precharged specimens

A quantity proposed as the measure of delayed fracture is the hydrogen concentration in the material. The idea is intuitively natural in cases where hydrogen plays a decisive role in fracture. Suzuki et al. measured the time to fracture under constant loading for hydrogen-precharged martensitic steel [80]. The initial hydrogen concentration was



controlled by varying HCl concentrations in aqueous solutions to dip the specimens, and the time to fracture was longer by decreasing the initial hydrogen concentration. Suzuki et al. defined the initial hydrogen concentration that did not cause fracture until 100 h as the critical hydrogen concentration  $H_C$  of the specimen at the applied stress. The hydrogen concentration was measured using thermal desorption analysis (TDA), which exhibited two desorption peaks. The higher temperature peak was likely an artifact in the experiment, and Suzuki et al. employed the lower temperature peak as meaningful diffusible hydrogen.

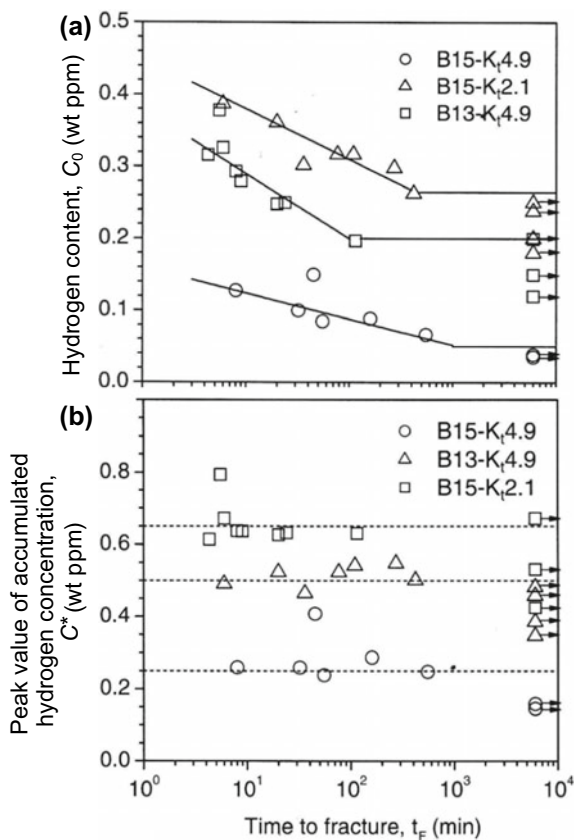
Yamazaki and Takahashi refined the method [81]; (1) hydrogen precharging and enclosing using cathodic electrolysis in a 3% NaCl + 3 g/l  $\text{NH}_4\text{SCN}$  aqueous solution at 0.5–10 A/m<sup>2</sup> followed by Cd plating, (2) the applied stress in delayed fracture at 0.9 of the ultimate tensile strength, confirming the failure of more than 99% of specimens within 50 h. Yamazaki et al. considered that failure in engineering service occurs when the amount of hydrogen from the environment,  $H_E$ , exceeds  $H_C$ . Since  $H_E$  varies with materials and environments, the meaningful measure is the difference between  $H_C$  and  $H_E$  at use, not  $H_C$  itself. Yamazaki et al. estimated  $H_E$  using a laboratory cyclic corrosion test (CCT) without applying stress and compared the laboratory and statistical failure frequencies in atmospheric exposure for several high-strength steels. A pretty good correspondence to the statistical result was found for a parameter  $(H_C - H_E)/H_C$ . The meaning of the parameter, rather than  $(H_C - H_E)$ , is not definite. The strength of each steel was different, and the orders of  $H_C$  and the statistical failure frequency were the same as the orders of the strength, implying a simple dependence on the strength level in the case.

Thus determined  $H_C$  is a phenomenological quantity averaged over an entire specimen. Delayed fracture is sensitive to specimen geometries, like the notch sharpness. As a criterion of the local crack initiation, Takagi et al. proposed the local critical hydrogen concentration  $H_C^*$ , estimated at the maximum hydrostatic stress site in front of the crack [82]. Takagi et al. further considered the stress distribution in front of the crack and proposed to take the average in a certain high-stress area, similar to the idea of process zone in fracture mechanics, at the crack front [83].

Within the scope of laboratory tests, the local hydrogen concentration well corresponds to the time-to-fracture diagram in delayed fracture. Figure 6.32(a) shows the time to fracture under a constant load test of high-strength martensitic steel [84]. Two levels of the ultimate tensile strength  $\sigma_B$ , 1450 and 1320 MPa, were prepared by varying tempering temperatures. The specimens were circumferentially notched round bars, and the notch-root radius was varied to give the stress concentration factors  $K_t$  of 2.1 and 4.9. Hydrogen precharging was by cathodic electrolysis in a 0.1 N NaOH aqueous solution at the current density of 0.3–10 A/m<sup>2</sup> for 48 h, and following cadmium plating prevented hydrogen release. The constant load test was at 0.9  $\sigma_B$  at the notch-root section.

In Fig. 6.32(a), the time to fracture increased with decreasing hydrogen content, and  $H_C$  was lower for higher  $K_t$  or the strength level. During constant loading, enclosed hydrogen accumulates at the site of the maximum hydrostatic stress. Wang et al. calculated the local hydrogen concentration by diffusion at the time of fracture [84]. Figure 6.32(b) plots the maximum local hydrogen concentration in Fig. 6.32(a)

**Fig. 6.32** (a) Constant load tests for the AISI 4135 steel at two strength levels and with two stress concentration factors. (b) Calculated peak values of the accumulated hydrogen concentration at the time of fracture or after loading for 6000 min for the specimens shown in (a) (Wang et al. [84])



for different initial hydrogen concentrations. The peak value of the accumulated hydrogen concentration at the time of fracture was almost constant, indicating that  $H_C^*$  is decisive for the occurrence of fracture in this case. The incubation time is the time spent for enough hydrogen to accumulate at the crack site.

### 6.4.5 Concept of the Critical Hydrogen Concentration

#### 6.4.5.1 Limitation as Fracture Criterion

Above cited Wang’s results [84] demonstrated that  $H_C^*$  is the decisive measure of delayed fracture in their test method.  $H_C^*$  is not a material constant and varies with testing conditions. In their case that uses hydrogen-precharged specimens, internal hydrogen diffusion increased the local hydrogen concentration with time.

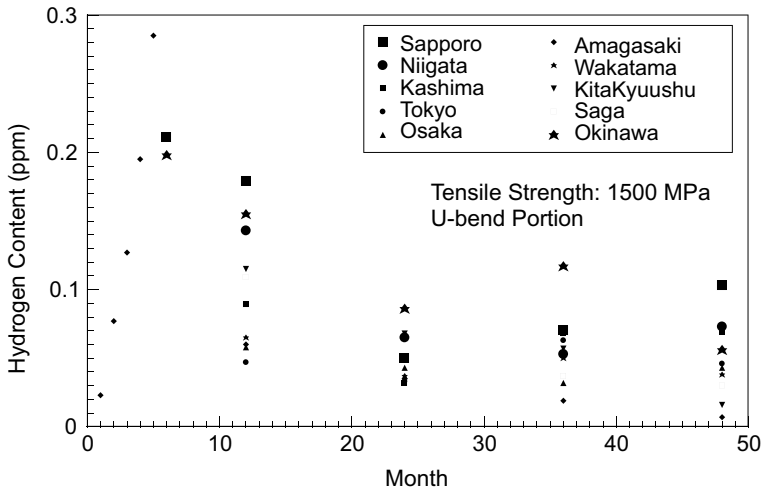


**Fig. 6.33** Hydrogen contents in U-bend loaded high-strength steel sheets of 1500 MPa in tensile strength after exposure at various sites in Japan (Kushida [85]. Reprinted with permission from The Iron and Steel Institute Japan)

The buildup of hydrogen concentration to a critical value is a widely adopted explanation of delayed fracture, but often without microscopic details of its function in fracture.

Reported data of hydrogen concentration in structural components exposed to environments for the long term are few. The entry of hydrogen from atmospheric environments was investigated at various sites in Japan for four years, and Fig. 6.33 shows the results [85]. The specimens were U-shape bent 1500 MPa high-strength steel plate of 3 mm in thickness. Hydrogen contents were measured using TDA as the amounts of hydrogen desorbed up to 473 K, at which the desorption almost ceased.

The increase in the hydrogen content in the initial six months was as expected, but further exposure decreased hydrogen content to a constant level. Data scattered substantially by the exposure sites, but systematic effects of local climates were not discernible. The facts are against the common notion of time-dependent hydrogen accumulation and imply that hydrogen contents are not always the decisive factor in causing delayed fracture under long atmospheric exposure.

Hydrogen entry initially increasing and then turning to decrease in sustained loading was also observed in laboratory tests. Figure 6.34 shows the time dependence of hydrogen contents during immersion in a 20%  $\text{NH}_4\text{SCN}$  aqueous solution at 323 K for 0.33% C martensitic steel bars of 5 mm in diameter [86]. The order of the increase in hydrogen content among three conditions, i.e., (○) unstressed, (▲) prestressed at 80% of the tensile strength, or (■) under sustained-loading, corresponds to the order of strain-induced creation of lattice defects and its enhancement by hydrogen, described concerning Fig. 3.10 in Sect. 3.2.3.2.

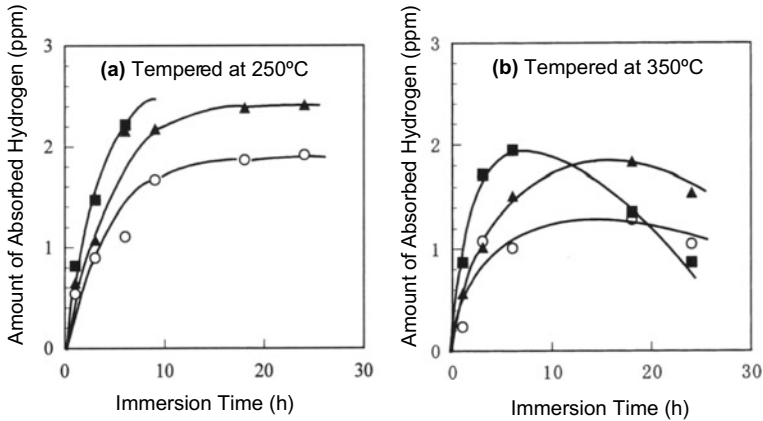


**Fig. 6.34** Amounts of absorbed hydrogen in medium-carbon tempered martensitic steels during immersion in 20%  $\text{NH}_4\text{SCN}$  aqueous solution at 323 K (50 °C).  $\circ$ : unloaded,  $\blacktriangle$ : prestressed to 80% of the tensile strength,  $\blacksquare$ : concurrently loaded to 80% of the tensile strength. (a) Tempered at 523 K (250 °C), (b) tempered at 623 K (350 °C) (Nagumo et al. [86])

The initial increase in hydrogen content was not monotonic in the steel tempered at 623 K, as shown in Fig. 6.34(b). Hydrogen content turned to decrease with increasing loading time. The TDA profile of absorbed hydrogen for each condition exhibited a single broad peak between 323 and 473 K. A comparison of TDA profiles for the three conditions indicated that the higher temperature side of the TDA peak concerns the increased hydrogen contents. The evolution in the higher temperature side implies the formation of traps with high binding energies with hydrogen during immersion, as described in Sect. 2.1.2. The reason for the decrease in hydrogen content is not definite, but the exchange of external and internal hydrogen occurs to keep equilibrium, reflecting changes in trapping states. Alterations of strain-induced defects during delayed fracture tests have been discussed with respect clustering of vacancies [86].

#### 6.4.5.2 Evaluation: Characterization or Assessment

Delayed fracture test methods developed in Refs. [81, 82, 84] were standardized by the International Organization for Standardization (ISO) [87]. The method is entitled “for evaluation of delayed fracture resistance”, but the document is limited in describing procedures to determine  $H_C$ . When  $H_C$  is the decisive factor for delayed fracture of a material,  $H_C$  is a quantitative expression *characterizing* delayed fracture of the material. In this meaning, the procedures to determine  $H_C$  are worthy as an evaluation method. However, the *qualification* of thus characterized material or *assessing* the material’s performance in engineering service is out of scope.

A further simplified proposal was a conventional strain-rate technique (CSRT) for evaluating delayed fracture [88]. The underlying idea might be that  $H_C$  or  $H_C^*$  under

stress is decisive generally and common in HE and must be identical in different loading methods. Accordingly, provided enough hydrogen comparable to  $H_C^*$  is present, the fracture condition obtained by a conventional strain-rate tensile test must be the same as those in a slow strain-rate tensile test or sustained-loading delayed fracture. The strain-rate and temperature effects on HE originates in the interaction between hydrogen and dislocation dynamics. The idea of CSRT lacks material aspects, such as microstructural alterations during straining and events that occur in the incubation period in delayed fracture. The CSRT is a proposal of a procedure to determine  $H_C^*$ , but its use for assessing the safety or reliability of material remains another subject.

The comparison of  $H_C$  and  $H_E$ , proposed by Yamazaki et al. [81], was to assess the safety of steel in engineering service. However, proper assessments so far published for engineering services are few. As described in the preceding Sect. 6.4.5.1, hydrogen contents from the environment do not monotonically increase during the incubation time, against the presumption in laboratory tests. The concept of the critical hydrogen concentration is not always proper as the fracture criterion.

When reliable empirical data for safe use are lacking, an alternative approach to assessing materials' quality should be based on the materials' intrinsic response to the operation of hydrogen causing embrittlement. The microscopic process that causes degradation of the material proceeds prior to the crack initiation, as described in Sects. 7.3 and 7.4. Based on these findings, Nagumo and Takai proposed a method to assess the intrinsic susceptibility to hydrogen embrittlement [89], described in Sect. 11.4.

## References

1. K. Takai, R. Watanuki, ISIJ Int. **43**, 520–526 (2003)
2. T. Doshida, K. Takai, Acta Mater. **79**, 93–107 (2014)
3. I.M. Bernstein, in *Hydrogen Effects in Materials*, ed. by A.W. Thompson, N.R. Moody (TMS, Warrendale PA, 1996), pp. 3–11
4. K. Takai, H. Suzuki, M. Fujinami, in *Reports on Construction of Fundamentals of Hydrogen Embrittlement* (Iron and Steel Institute Japan, 2013), pp. 129–134
5. T. Nakamoto, T. Doshida, K. Takai, Y. Kubo, M. Fujinami, CAMP ISIJ25 (2012), p. 1210
6. K. Takai, H. Shoda, H. Suzuki, M. Nagumo, Acta Mater. **56**, 5158–5167 (2008)
7. M. Hatano, M. Fujinami, K. Arai, H. Fujii, M. Nagumo, Acta Mater. **67**, 342–353 (2014)
8. J.F. Knott, *Fundamentals of Fracture Mechanics* (Butterworth, London, 1973)
9. T.L. Anderson, *Fracture Mechanics*, 3rd edn. (Taylor & Francis, Boca Raton, FL, USA, 2005)
10. W.G. Clark Jr., J. Mater. Energy Syst. **1**, 34–40 (1979)
11. R.A. Oriani, P.H. Josephic, Acta Metall. **22**, 1065–1074 (1974)
12. G.W. Simmons, P.S. Pao, R.P. Wei, Metall. Trans. A **9A**, 1147–1158 (1978)
13. W.W. Gerberich, Y.T. Chen, and C. ST. John: Metall. Trans. A **6A**, 1485–1498 (1975)
14. J.F. Lessar, W.W. Gerberich, Metall. Trans. A **7A**, 953–960 (1976)
15. N.R. Moody, S.L. Robinson, W.M. Garrison, Res Mechanica **30**, 143–206 (1990)
16. Y. Takeda, C.J. McMahon, Jr., Metall. Trans. A, **12(A)**, 1255–1266 (1981)
17. J.A. Gordon, J.P. Hirth, A.M. Kumar, N.E. Moody Jr., Metall. Trans. A **23A**, 1013–1020 (1992)
18. S.V. Kamat, J.P. Hirth, Scr. Metal. Mater. **30**, 145–148 (1994)

19. Y. Fujii, A. Kikuchi, M. Nagumo, *Metall. Mater. Trans. A* **27A**, 469–471 (1996)
20. A. Needleman, Tvergaard, *J. Mech. Phys. Solids*, **35**, 151–183 (1987)
21. Y. Shimomura, M. Nagumo, in *Environment-Induced Cracking of Materials: Chemistry, Mechanics and Mechanisms*, ed. by S.A. Shipilov, R.H. Jones, J.M. Olive, R.B. Rebak (Elsevier, Oxford, 2007), pp. 285–294
22. D.P. Williams, H.G. Nelson, *Metall. Trans.* **1**, 63–68 (1970)
23. R.P. Gangloff, R.P. Wei, *Metall. Trans. A* **8A**, 1043–1053 (1977)
24. H. Vehoff, W. Rothe, *Acta Metall.* **31**, 1781–1793 (1983)
25. H. Vehoff, H.-K. Llameth, *Acta Metall.* **33**, 955–962 (1985)
26. W.W. Gerberich, T. Livne, X.-F. Chen, M. Kaczorowski, *Metall. Trans. A* **19A**, 1319–1334 (1988)
27. M. Nagumo, T. Yagi, H. Saitoh, *Acta Mater.* **48**, 943–951 (2000)
28. H. Yoshida, M. Nagumo, *ISIJ Int.* **38**, 196–202 (1998)
29. M. Nagumo, H. Yoshida, Y. Shimomura, T. Kadokura, *Mater. Trans.* **42**, 132–137 (2001)
30. K.A. Nibur, B.P. Somerday, D.K. Balch, C. San Marchi, *Acta Mater.* **57**, 3795–3809 (2009)
31. R.W. Hertzberg, *Deformation and Fracture Mechanics of Engineering Materials 3rd Ed.* (John Wiley & Sons, N. Y. 1989), pp. 457–515, 517–604
32. W.W. Gerberich, in *Hydrogen Degradation of Ferrous Alloys*, eds. by R.A. Oriani, J.P. Hirth, M. Smialowski (Noyes Pub., Park Ridge NJ, 1985), pp. 366–413
33. Y. Murakami, H. Matsunaga, *Int. J. Fatigue* **28**, 1509–1520 (2006)
34. M. Nagumo, H. Shimura, T. Chaya, H. Hayashi, I. Ochiai, *Mater. Sci. Eng. A* **348**, 192–200 (2003)
35. H. Matsunaga, M. Yoshikawa, R. Kondo, J. Yamabe, S. Matsuoka, *Int. J. Hydrogen Energy* **40**, 5739–5748 (2015)
36. Y. Ogawa, H. Matsunaga, J. Yamabe, M. Yoshikawa, S. Matsuoka, *Int. J. Hydrogen Energy* **43**, 20133 e20142 h (2018)
37. N. Nanninga, A. Slifka, Y. Levy, C. White, *J. Res. Nat. Inst. Stand. Technol.* **115**, 437–452 (2010)
38. S. Suresh, G.F. Zamiski, And R. O. Ritchie: *Metall. Trans. A* **12A**, 1435–1443 (1981)
39. S. Suresh, R.O. Ritchie, *Scr. Metall.* **17**, 575–580 (1983)
40. S.J. Hudak Jr., *Trans. ASME J. Eng. Mater. Tech.* **103**, 26–35 (1981)
41. M.H. Haddad, N.E. Dowling, T.H. Topper, K.N. Smith, *Int. J. Fracture* **16**, 15–30 (1980)
42. K.A. Esaklul, A.G. Wright, W.W. Gerberich, *Scr. Metall.* **17**, 1073–1078 (1983)
43. S. Fukuyama, K. Yokogawa, M. Araki, *J. Soc. Mater. Sci. Jpn.* **34**, 709–714 (1985)
44. Y. Ogawa, D. Birenis, H. Matsunaga, O. Takakuwa, J. Yamabe, Ø. Prytz, A. Thøgersen, *Mater. Sci. Eng. A* **733**, 316–328 (2018)
45. J. Yamabe, M. Yoshikawa, H. Matsunaga, S. Matsuoka, *Int. J. Fatigue* **102**, 202–213 (2017)
46. Y. Ogawa, H. Nishida, M. Nakamura, V. Olden, A. Vinogradov, H. Matsunaga, *Int. J. Fatigue* **154**, 106561 (2022)
47. A. Setoyama, Y. Ogawa, M. Nakamura, Y. Tanaka, T. Chen, M. Koyama, H. Matsunaga, *Int. J. Fatigue*. <https://doi.org/10.1016/j.ijfatigue.2022.107039>
48. Y. Ogawa, K. Umakoshi, M. Nakamura, O. Takakuwa, H. Matsunaga, *Int. J. Fatigue* **140**, 105806 (2020)
49. S. Matsuoka, O. Takakuwa, S. Okazaki, M. Yoshikawa, J. Yamabe, H. Matsunaga, *Scripta Mater.* **154**, 101–105 (2018)
50. J. Yamabe, T. Matsumoto, S. Matsuoka, Y. Murakami, *Int. J. Fracture* **177**, 141–162 (2012)
51. Z. Sun, C. Moriconi, G. Benoit, D. Halm, G. Henaff, *Metall. Mater. Trans. A* **44A**, 1320–1330 (2013)
52. B.P. Somerday, P. Sofronis, K.A. Nibur, C. San Marchi, R. Kirchheim, *Acta Mater.* **61**, 6153–6170 (2013)
53. Y. Ogawa, O. Takakuwa, S. Okazaki, Y. Funakoshi, S. Matsuoka, H. Matsunaga, *Corros. Sci.* **174**, 108814 (2020)
54. Y. Murakami, T. Kanezaki, Y. Mine, *Metall. Mater. Trans. A* **41A**, 2548–2562 (2010)
55. S. Ohmiya, H. Fujii, *ASME Pressure Vessels and Piping Conf.* 2007–26492

56. J. Nakamura, M. Miyahara, T. Omura, H. Semba, M. Wakita, *J. Soc. Mater. Sci.* **60**, 1123–1129 (2011)
57. M. Yamamura, J. Nakamura, T. Omura, M. Hatano, *Tetsu-to-Hagane* **107**, 237–246 (2021)
58. S. Stanzl, E. Tschegg, *Acta Metall.* **29**, 21–32 (1981)
59. Y. Murakami, H. Konishi, K. Takai, Y. Murakami, *Tetsu-to-Hagane* **86**, 777–783 (2000)
60. P.C. Paris, *Fatigue Fract. Eng. Mater. Struct.* **21**, 535–540 (1998)
61. P. Paris, F. Erdogan, *Trans. ASME. J. Basic Eng.* **85**, 528–534 (1963)
62. A.K. Head, *The London, Edinburgh, and Dublin Philosophical Magazine and Journal of Science* **44**, 925–938 (1953)
63. R.J. Donahue, H. McI. Clark, P. Atanmo, R. Kumble, A.J. McEvily, *Int. J. Fract. Mech.*, **8**, 209–219 (1972)
64. J. Weertman, *Int. J. Fracture* **2**, 460–467 (1966)
65. J.D. Lee, H. Liebowitz, *Comput. Structures* **8**, 403–410 (1978)
66. S.R. Bodner, D.L. Davidson, J. Lankford, *Eng. Fract. Mech.* **17**, 189–191 (1983)
67. N.W. Klingbeil, *Int. J. Fatigue* **25**, 117–128 (2003)
68. J.A.R. Durán, J.T.P. Castro, J.C.P. Filho, *Fatigue Fract. Eng. Mater. Struct.* **26**, 137–150 (2003)
69. H.H. Johnson, J.G. Morlet, A.R. Troiano, *Trans. Metall. Soc. AIME* **212**, 528–536 (1958)
70. W.W. Gerberich, Y.T. Chen, *Metall. Trans. A* **6A**, 271–278 (1975)
71. E.A. Steigerwald, F.W. Schaller, A.R. Troiano, *Trans. Metall. Soc. AIME* **215**, 1048–1052 (1959)
72. M. Nagumo, in *Fracture 1977, Proceedings of 4th International Conference Fracture, vol.3*, ed. by D.M.R. Taplin (University Waterloo Press, Waterloo, Canada, 1977), pp. 757–764
73. S. Yamamoto, T. Fujita, *Kobe Steel. Tech. Rep.* **18**, 93–108 (1968)
74. M. Nagumo, T. Tamaoki, T. Sugawara, in *Hydrogen Effects on Materials Behavior and Corrosion Deformation Interactions*, eds. by N.R. Moody, A.W. Thompson, R.E. Ricker, C.W. Was, K.H. Jones (TMS, Warrendale PA, 2003), pp. 999–1008
75. K. Nakasa, M. Kido, H. Takei, *J. Jpn Inst. Metals* **40**, 744–751 (1976)
76. M. Kido, K. Nakasa, H. Takei, *Tetsu-to-Hagane* **65**, 535–541 (1979)
77. K. Izutsu, K. Takai, M. Nagumo, *Tetsu-to-Hagane* **83**, 371–376 (1997)
78. M. Nagumo, H. Uyama, M. Yoshizawa, *Scr. Mater.*, **44**, 947–952 (2001)
79. Technical Report, Reports on Prestressing Steel: 5. Stress corrosion cracking resistance test for prestressing tendons, *Fédération Internationale de la Précontrainte*, Slough (1980)
80. N. Suzuki, N. Ishii, T. Miyagawa, H. Harada, *Tetsu-to-Hagane* **79**, 227–232 (1993)
81. S. Yamazaki, T. Takahashi, *Tetsu-to-Hagane* **83**, 454–459 (1997)
82. S. Takagi, T. Inoue, T. Hara, M. Hayakawa, K. Tsuzaki, T. Takahashi, *Tetsu-to-Hagane* **86**, 689–695 (2000)
83. S. Takagi, S. Terasaki, K. Tsuzaki, T. Inoue, F. Minami, *ISIJ Int.* **45**, 263–271 (2005)
84. M. Wang, E. Akiyama, K. Tsuzaki, *Corros. Sci.* **48**, 2189–2202 (2006)
85. T. Kushida, *ISIJ Int.* **43**, 470–474 (2003)
86. M. Nagumo, M. Nakamura, K. Takai, *Metall. Mater. Trans. A* **32A**, 339–346 (2001)
87. ISO 16573:2015
88. Y. Hagihara, T. Shobu, N. Hisamoro, H. Suzuki, K. Takai, K. Hirai, *ISIJ Int.* **52**, 298–306 (2012)
89. M. Nagumo, K. Takai, *Mater. Sci. Tech.* **36**, 1003–1011 (2020)